Cell

Atlas of Subcellular RNA Localization Revealed by APEX-Seq

Graphical Abstract

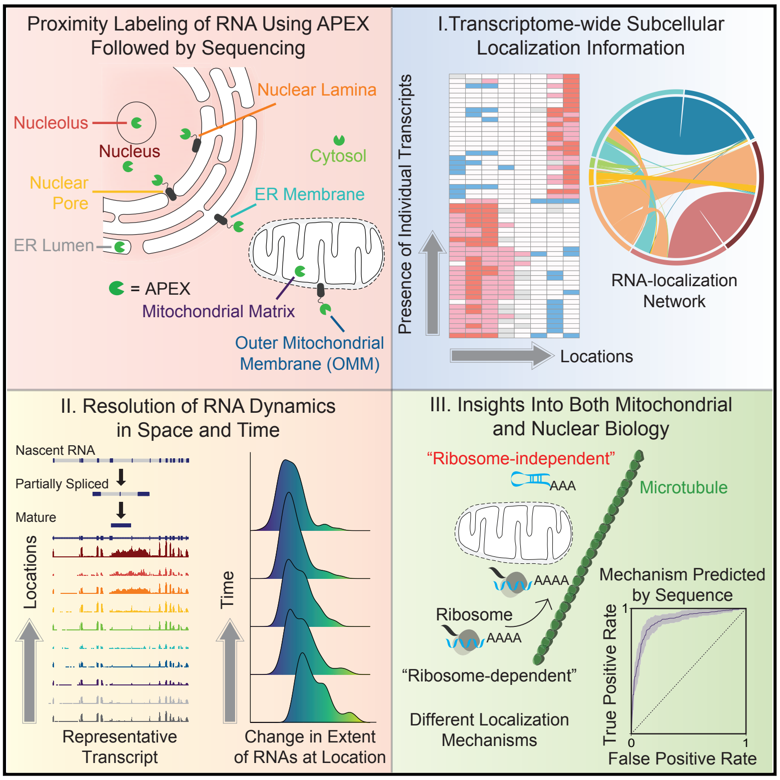
Proximity Labeling of RNA Using APEX Followed by Sequencing
Nuclear Lamina
Nucleolus
Nucleus
Cytosol
Nuclear Pore
ER Membrane
ER Lumen
= APEX
Mitochondrial Matrix
Outer Mitochondrial Membrane (OMM)
I.Transcriptome-wide Subcellular Localization Information
Presence of Individual Transcripts
Locations
RNA-localization Network
II. Resolution of RNA Dynamics in Space and Time
Nascent RNA
Partially Spliced
Mature
Locations
Time
Representative Transcript
Change in Extent of RNAs at Location
III. Insights Into Both Mitochondrial and Nuclear Biology
"Ribosome-independent"
AAA
Microtubule
AAAA
Ribosome
AAAA
"Ribosome-dependent"
Mechanism Predicted by Sequence
True Positive Rate
1
0
1
False Positive Rate
Different Localization Mechanisms

Highlights

- A transcriptome-wide subcellular RNA atlas was generated by proximity labeling
- Isoform-level subcellular localization patterns for over 3,200 genes identified
- RNA-transcript location correlates with genome architecture and protein localization
- Two modes of mRNA localization to the outer mitochondrial membrane uncovered

Authors

Furqan M. Fazal, Shuo Han,
Kevin R. Parker, ..., Alistair N. Boettiger,
Howard Y. Chang, Alice Y. Ting

Correspondence

howchang@stanford.edu (H.Y.C.),
ayting@stanford.edu (A.Y.T.)

In Brief

A newly developed technique reveals the subcellular transcriptomes at many landmarks in the nucleus and cytosol and connects mRNA localization to genome architecture, protein location, and local-translation mechanisms.

Fazal et al., 2019, Cell *178*, 473–490
July 11, 2019 © 2019 Elsevier Inc.
https://doi.org/10.1016/j.cell.2019.05.027

CellPress

Atlas of Subcellular RNA Localization Revealed by APEX-Seq

Furqan M. Fazal,[1,2,3,9] Shuo Han,[3,4,5,9] Kevin R. Parker,[1,2,3,10] Pornchai Kaewsapsak,[3,4,5,10] Jin Xu,[1,2,3]
Alistair N. Boettiger,[6] Howard Y. Chang,[1,2,3,7,*] and Alice Y. Ting[3,4,5,8,11,*]
[1]Center for Personal Dynamics Regulomes, Stanford University School of Medicine, Stanford, CA 94305, USA
[2]Department of Dermatology, Stanford University School of Medicine, Stanford, CA 94305, USA
[3]Department of Genetics, Stanford University School of Medicine, Stanford, CA 94305, USA
[4]Department of Chemistry, Stanford University, Stanford, CA 94305, USA
[5]Department of Biology, Stanford University, Stanford, CA 94305, USA
[6]Department of Developmental Biology, Stanford University School of Medicine, Stanford, CA 94305, USA
[7]Howard Hughes Medical Institute, Stanford University School of Medicine, Stanford, CA 94305, USA
[8]Chan Zuckerberg Biohub, San Francisco, CA 94158, USA
[9]These authors contributed equally
[10]These authors contributed equally
[11]Lead Contact
*Correspondence: howchang@stanford.edu (H.Y.C.), ayting@stanford.edu (A.Y.T.)

https://doi.org/10.1016/j.cell.2019.05.027

SUMMARY

We introduce APEX-seq, a method for RNA sequencing based on direct proximity labeling of RNA using the peroxidase enzyme APEX2. APEX-seq in nine distinct subcellular locales produced a nanometer-resolution spatial map of the human transcriptome as a resource, revealing extensive patterns of localization for diverse RNA classes and transcript isoforms. We uncover a radial organization of the nuclear transcriptome, which is gated at the inner surface of the nuclear pore for cytoplasmic export of processed transcripts. We identify two distinct pathways of messenger RNA localization to mitochondria, each associated with specific sets of transcripts for building complementary macromolecular machines within the organelle. APEX-seq should be widely applicable to many systems, enabling comprehensive investigations of the spatial transcriptome.

INTRODUCTION

The subcellular localization of RNA is intimately tied to its function (Buxbaum et al., 2015). Asymmetrically distributed RNAs underlie organismal development, local protein translation, and the 3D organization of chromatin. Where an RNA is located within the cell likely determines whether it will be stored, processed, translated (Berkovits and Mayr, 2015), or degraded (Fasken and Corbett, 2009).

While many methods have been developed to study RNA localization (Weil et al., 2010), only a few have been applied on a transcriptome-wide scale. The most classic approach is biochemical fractionation to enrich specific organelles, followed by RNA sequencing (“fractionation-seq”). However, a major limitation of fractionation-seq is that it cannot be applied to organelles that are impossible to purify, such as the nuclear lamina and outer mitochondrial membrane (OMM). Even for organelles that *can* be enriched by centrifugation, such as mitochondria, current protocols fail to remove contaminants (Sadowski et al., 2008).

RNA localization can also be directly visualized by microscopy (Bertrand et al., 1998; Femino et al., 1998), and techniques have recently been pioneered for imaging thousands of cellular RNAs at once using barcoded oligonucleotides (Chen et al., 2015b; Shah et al., 2016). The drawbacks of these fluorescence *in situ* hybridization (FISH)-based approaches, however, are the need for designed probe sets targeting RNAs of interest; the requirement for cell fixation and permeabilization, which can relocalize cellular components (Fox et al., 1985; Schnell et al., 2012); the difficulty of assigning RNAs to specific cellular landmarks due to spatial resolution limits; and the limited information content compared to RNA sequencing. Finally, these transcriptome-wide imaging methods are technically challenging and require specialized instrumentation not available to most.

An adaptation of ribosome profiling (Ingolia et al., 2009) has enabled this technique to profile actively translated mRNAs in specific cellular locales. The two demonstrations—on the endoplasmic reticulum membrane (ERM) in yeast and mammalian cells (Jan et al., 2014), and on the OMM in yeast (Williams et al., 2014)—showed high spatial specificity and compatibility with living cells. However, the methodology cannot detect non-coding RNAs or non-translated mRNAs. Proximity-specific ribosome profiling is also not yet a fully generalizable method, as the requirement for biotin starvation during cell culture is prohibitively toxic to many cell types.

Hence, there remains a need for new methodology that can map the spatial localization of thousands of endogenous RNAs at once in living cells. The method should be applicable to any subcellular region and capture full sequence details of any RNA type, enabling comparisons across RNA variants and isoforms. Here, we develop the “APEX-seq” methodology in an effort to provide these capabilities. We characterize the

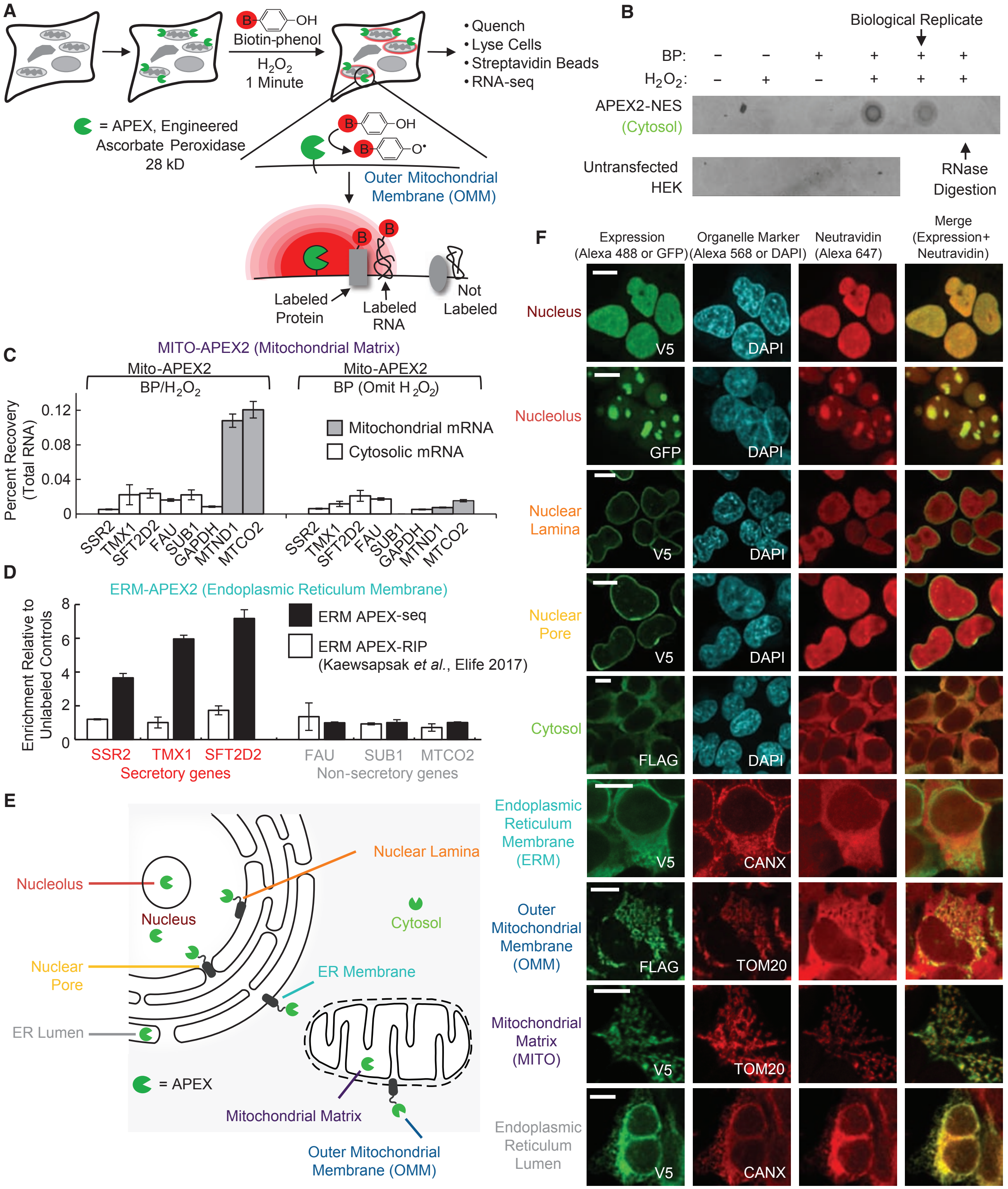

Figure 1. Development of APEX-Seq Methodology

(A) APEX2-mediated proximity biotinylation of endogenous RNAs. APEX2 peroxidase is genetically targeted to the cellular region of interest. Addition of BP (red B = biotin) and H_2O_2 to live cells for 1 min results in biotinylation of endogenous proteins and RNA within a few nanometers of APEX2. Biotinylated RNAs are separated using streptavidin-coated beads, poly(A)-selected, and analyzed by RNA sequencing (RNA-seq).

(legend continued on next page)

APEX-seq approach and then apply it to nine subcellular locations, generating a high-resolution atlas of endogenous RNA localization in living human HEK293T cells. Our data reveal correlations between localization of mRNAs and the protein products they encode, as well as patterns of RNA localization and underlying genome architecture. An analysis of mRNAs at the OMM suggests distinct mechanisms for RNA targeting that correlate with the sequence and function of the encoded mitochondrial proteins. These examples illustrate the versatility of APEX-seq and its ability to nominate or test novel biological hypotheses.

RESULTS

APEX-Catalyzed Labeling of RNA

To develop the methodology, we drew from previous work in our laboratory using enzymes to map spatial proteomes (Rhee et al., 2013). APEX2 (Lam et al., 2015) is an evolved mutant of soybean ascorbate peroxidase that catalyzes the one-electron oxidation of biotin-phenol (BP), a membrane-permeable small molecule. The resulting BP radical is short-lived (half-life <1 ms) (Mortensen and Skibsted, 1997; Wishart and Rao, 2010) and covalently conjugates onto protein side chains. Hence, APEX2 catalyzes the promiscuous biotin tagging of endogenous proteins within a few nanometers of its active site in living cells. The high spatial specificity of this approach has enabled APEX mapping of numerous organelle proteomes as well as protein interaction networks (Han et al., 2018).

We previously combined APEX proteomic tagging with formaldehyde protein-RNA crosslinking in order to extend our analysis to cellular RNAs (Kaewsapsak et al., 2017). While this “APEX-RIP” approach was effective at mapping the RNA composition of membrane-enclosed organelles such as the mitochondrion, its spatial specificity was poor in “open” or non-membrane enclosed cellular regions. For instance, RNAs enriched by APEX targeted to the ERM (facing cytosol) were no different from those enriched by cytosolic APEX. A version of this two-step strategy using UV crosslinking may improve specificity (Benhalevy et al., 2018).

A more straightforward and potentially higher-specificity approach would be to bypass crosslinking altogether and use APEX peroxidase to directly biotinylate cellular RNAs within a short time window (Figure 1A). To test whether peroxidase-generated phenoxyl radicals could biotinylate RNA *in vitro*, we combined horseradish peroxidase (HRP), which catalyzes the same one-electron oxidation chemistry as APEX2, with tRNA, BP, and H_2O_2. On a streptavidin dot blot, we observed robust tRNA biotinylation that was abolished by RNase treatment but unaffected by proteinase K treatment (Figure S1A). We next used a RT stop assay to evaluate the labeling and found that, while full-length transcripts are still produced, multiple RT stops are observed at G-rich regions in peroxidase-catalyzed RNA samples (Figures S1D and S1E). Additional experiments characterized the covalent adduct between G and BP by HPLC and mass spectrometry (Figures S1B and S1C).

To test APEX-catalyzed RNA biotinylation in living cells, we generated HEK cells stably expressing APEX2 in the cytosol. We labeled the cells with BP and H_2O_2 for 1 min, extracted total RNA, and analyzed the RNA by streptavidin dot blot. Figure 1B shows that RNA biotinylation is abolished upon omission of BP or H_2O_2 or following treatment with RNase. Combined with the assays above, our results suggest that APEX directly tags RNA with biotin, not merely biotinylating proteins co-complexed with RNA.

Next, we combined APEX labeling with qRT-PCR analysis of biotinylated RNAs in order to begin assessing the spatial specificity of this approach. We started with the mitochondrial matrix, which we have previously characterized by APEX proteomics (Han et al., 2017; Rhee et al., 2013), and whose transcriptome can be predicted by the sequence of the mitochondrial genome (mtDNA) (Mercer et al., 2011). Using HEK cells expressing APEX2 in the mitochondrial matrix, we performed labeling and then extracted RNA and enriched the biotinylated fraction using streptavidin beads. We optimized a series of denaturing washes to fully dissociate complexes and ensure that the streptavidin beads only enriched biotinylated RNA species (Figure S1F). We then analyzed the eluate by qRT-PCR and observed strong enrichment of mtDNA-encoded mRNAs *MTND1* and *MTCO2* but not negative-control cytosolic mRNAs (Figure 1C).

However, because the mitochondrial matrix is enclosed by a tight membrane that is impervious to BP radicals (Rhee et al., 2013), it does not provide a rigorous test of APEX labeling radius. To evaluate spatial specificity in an open cellular compartment, we utilized HEK cells stably expressing APEX2 on the ERM, facing cytosol. qRT-PCR analysis of streptavidin-enriched RNA following BP labeling (Figure 1D) shows high enrichment of secretory mRNAs (ERM-proximal ‘‘true positives’’) but not negative-control cytosolic mRNAs (encoding non-secretory proteins). This result suggests that APEX biotinylation has nanometer spatial resolution and is able to distinguish ER-proximal RNAs

(B) Streptavidin-biotin dot-blot analysis of direct RNA biotinylation by APEX2 in cells. HEK-293T cells expressing APEX2 in the cytosol were labeled with for 1 min and then the RNA was extracted and blotted. Only when BP, H_2O_2, and APEX2 were all present was the signal observed. RNase treatment of the sample abolished the signal.

(C) qRT-PCR analysis showing specific enrichment of mitochondrial RNAs (gray) over cytosolic mRNAs (white). Cells expressing APEX2 targeted to the mitochondrial matrix were labeled for 1 min. Biotinylated RNAs were enriched following RNA extraction. Data are the mean of 4 replicates ± 1 SD.

(D) qRT-PCR analysis showing specific enrichment of secretory (red) over non-secretory (gray) mRNAs with APEX-seq, but not APEX-RIP. Cells stably expressing APEX2 targeted to the ERM membrane (facing cytosol) were labeled for 1 min. For APEX-RIP, RNAs were crosslinked to proteins for 10 min before streptavidin beads enrichment. Data are the mean of 4 replicates ±1 SD. The data were normalized such that the mean enrichment of non-secretory RNAs was 1 for both techniques.

(E) Human cell showing nine different subcellular locations investigated.

(F) Fluorescence imaging of APEX2 localization and biotinylation activity. Live-cell biotinylation was performed for 1 min in cells stably expressing the indicated APEX2 fusion protein. APEX2 expression was visualized by GFP or antibody staining (green). Biotinylation was visualized by staining with neutravidin-Alexa Fluor 647 (red). DAPI is a nuclear marker. Endogenous *TOM20* and *CANX* were used as markers for the mitochondria and ER, respectively. Scale bars, 10 μm.
See also Figure S1 and Table S1.

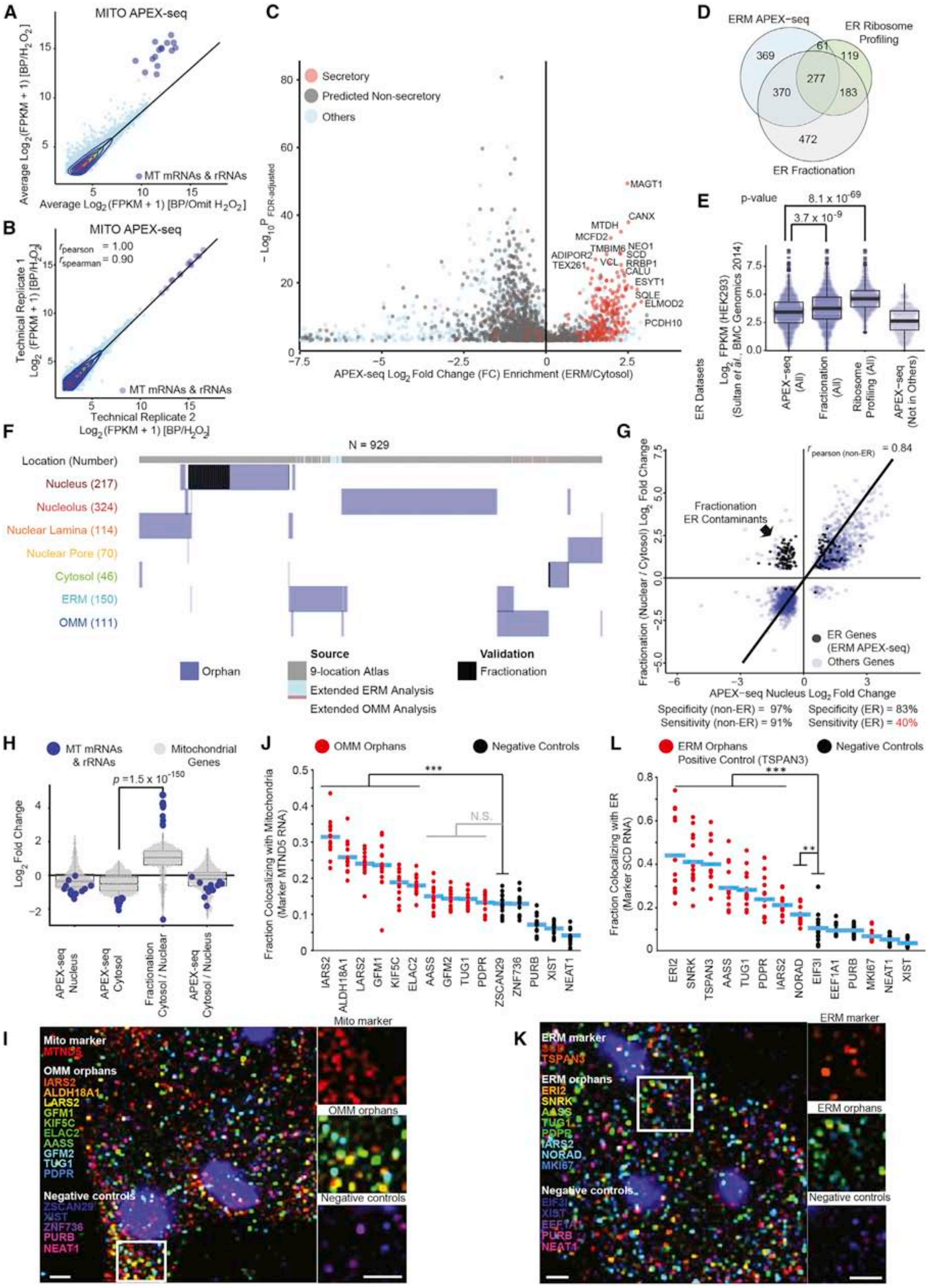

(legend on next page)

from cytosolic RNAs only nanometers from the ERM. This result strikingly contrasts with previous observations using APEX-RIP (Kaewsapsak et al., 2017). For a further side-by-side comparison between APEX-seq and APEX-RIP, a total of 8 representative transcripts that are known to localize to the respective landmarks based on previous literature, were investigated by qRT-PCR (Figure S2E). APEX-seq enriched specific, proximal RNAs in open subcellular regions (ERM, nuclear lamina, nucleolus, and OMM), whereas APEX-RIP was unable to do so.

Development and Validation of APEX-Seq

Encouraged by the results above, we moved to a more comprehensive analysis by replacing qRT-PCR with transcriptome-wide sequencing. We also created cell lines expressing APEX in nine subcellular locales (Figures 1E and S2A). For each cell line, we verified correct targeting of APEX by performing immunofluorescence staining against organelle markers. To examine APEX activity, we performed BP labeling, fixed, and stained the biotinylated species using neutravidin-Alexa 647. For some locations, the neutravidin pattern overlapped closely with APEX localization (e.g., nucleolus and mitochondrial matrix; Figure 1F), indicating minimal diffusion of biotinylated species. For other locations, the neutravidin signal was more “spread out” than the APEX signal (e.g., ERM and OMM; Figure S2B), suggesting redistribution of biotinylated species during the 1-min labeling time window (Hung et al., 2016).

To assess the quality of the poly(A)-selected APEX-seq data (Figures S2C and S2D; Table S2), we first focused on two subcellular compartments that have been extensively mapped: the mitochondrial matrix and the ERM. For the former (Figures 2A and 2B), APEX-seq experiments showed strong enrichment of all 13 mRNAs and the 2 rRNAs encoded by mtDNA (Figures S2F and S2G), while no RNAs encoded by the nuclear genome were highly enriched.

For the ERM, APEX-seq highly enriched RNAs previously shown to be ER proximal (such as mRNAs encoding secreted proteins) over cytosol-localized RNAs. To perform a quantitative analysis, we used ROC cutoff analysis (Linden, 2006) (Figures S2I and S2J) to produce a list of 1,077 ERM-enriched RNAs (Figure 2C). To evaluate the specificity of this dataset, we determined the fraction of “secretory” or “transmembrane” mRNAs (STAR Methods) and found that 90% of genes had such prior annotations. The remaining 10% (107 genes) could be false-positives, or they could be newly discovered ERM-associated RNAs.

To evaluate depth of coverage, we prepared a hand-curated list of 71 well-established ER-resident proteins and asked what fraction of their corresponding mRNAs appear in our ERM APEX-seq dataset. We recovered 70% of this true-positive list (Figure S2K). This sensitivity is comparable to that of our previous APEX proteomic datasets in open compartments (Hung et al., 2017) (Figure S2L). RNAs we failed to enrich could be sterically shielded in the live cell environment, low in abundance, or dual-localized to both ERM and cytosol.

The ERM-associated transcriptome has previously been studied by fractionation-seq (Reid and Nicchitta, 2012) and proximity-specific ribosome profiling (Jan et al., 2014). Upon analyzing the published datasets, we found that the specificities of fractionation-seq and APEX-seq were comparably high (90% versus 91% secretory mRNAs, respectively; Figure S2I), in addition to sensitivity (Figure S2K). However, Figure 2D shows that each method recovers somewhat different subsets of transcripts. Further analysis of genes enriched by APEX-seq but *not* fractionation-seq or ribosome profiling show that many of these are lower in RNA abundance (Figure 2E).

Altogether, our APEX-seq analysis demonstrates that high specificity and reasonable sensitivity can be achieved in both membrane-enclosed and open subcellular compartments.

RNA Atlas of 9 Distinct Subcellular Compartments by APEX-Seq

Having established the specificity and sensitivity of APEX-seq using the mitochondrial matrix and ERM, we turned our attention to the seven other compartments (Figure 1E). The RNA content of most of these regions has not previously been mapped, as

Figure 2. Validation of APEX-Seq, Including Specific Orphans from RNA Atlas

(A) APEX-seq in the mitochondrial matrix. Transcript abundance in experiment plotted against negative control (omit H_2O_2). All mRNAs and rRNAs encoded by the mitochondrial genome (large blue dots) are enriched by APEX (mean enrichment >11-fold). FPKM, fragments per kilobase of transcript per million reads. Due to the 100-nt size selection step during RNA extraction, tRNAs were not efficiently recovered.

(B) Scatterplot of transcript abundance in the mitochondrial matrix (MITO).

(C) APEX-seq at the ERM, facing cytosol. Volcano plot showing APEX-catalyzed enrichment of secretory mRNAs (red) over non-secretory mRNAs (black).

(D) Comparison of ERM-enriched RNAs by APEX-seq, proximity-specific ribosome profiling, and ER fractionation-seq.

(E) Transcript abundance (FPKM) analysis of genes enriched by ERM APEX-seq, fractionation-seq, proximity-specific ribosome profiling, and genes unique to the APEX-seq dataset. p values are from a Mann-Whitney U test.

(F) Total number of orphans (blue) generated from APEX-seq RNA datasets, with those validated by further poly(A)+ fractionation-seq shown in black. The source of most of these RNAs is the RNA atlas, with further contributions from analysis of the ERM and OMM transcriptomes.

(G) APEX-seq yields cleaner results than bulk fractionation RNA-seq. Nucleus APEX-seq fold changes are highly correlated with bulk fractionation RNA-seq when considering non-ER genes (blue). However, fractionation suffers from contamination by ER transcripts (black).

(H) APEX-seq in the cytosol does not recover mitochondrial-genome encoded RNAs, whereas fractionation-seq does. mRNAs and rRNAs encoded by the mitochondrial genome are shown in blue, whereas mRNAs for mitochondrial proteins encoded by the nuclear genome are shown in grey. p value is from a Mann-Whitney U test.

(I and K) Sequential smFISH imaging of OMM (I) or ERM (K) orphans in HEK cells. MTND5 was used as a mitochondrial marker. SCD and TSPAN3 were used as ERM markers. mRNAs and lncRNAs not enriched in OMM (I) or ERM (K) were used as negative controls. Expanded views of the boxed region are shown on the right. Scale bar, 5 μm.

(J and L) Quantitation of OMM (J) or ERM (L) orphans colocalization with MTND5 (J) or SCD (L) by sequential smFISH imaging. Blue lines represent mean from 14 independent fields of view. Data were analyzed using a two-tailed Student’s t test, with $^*p < 0.05$, $^{**}p < 0.01$, and $^{***}p < 0.001$; N.S., not significant ($p > 0.05$). See also Figure S2 and Tables S2 and S3.

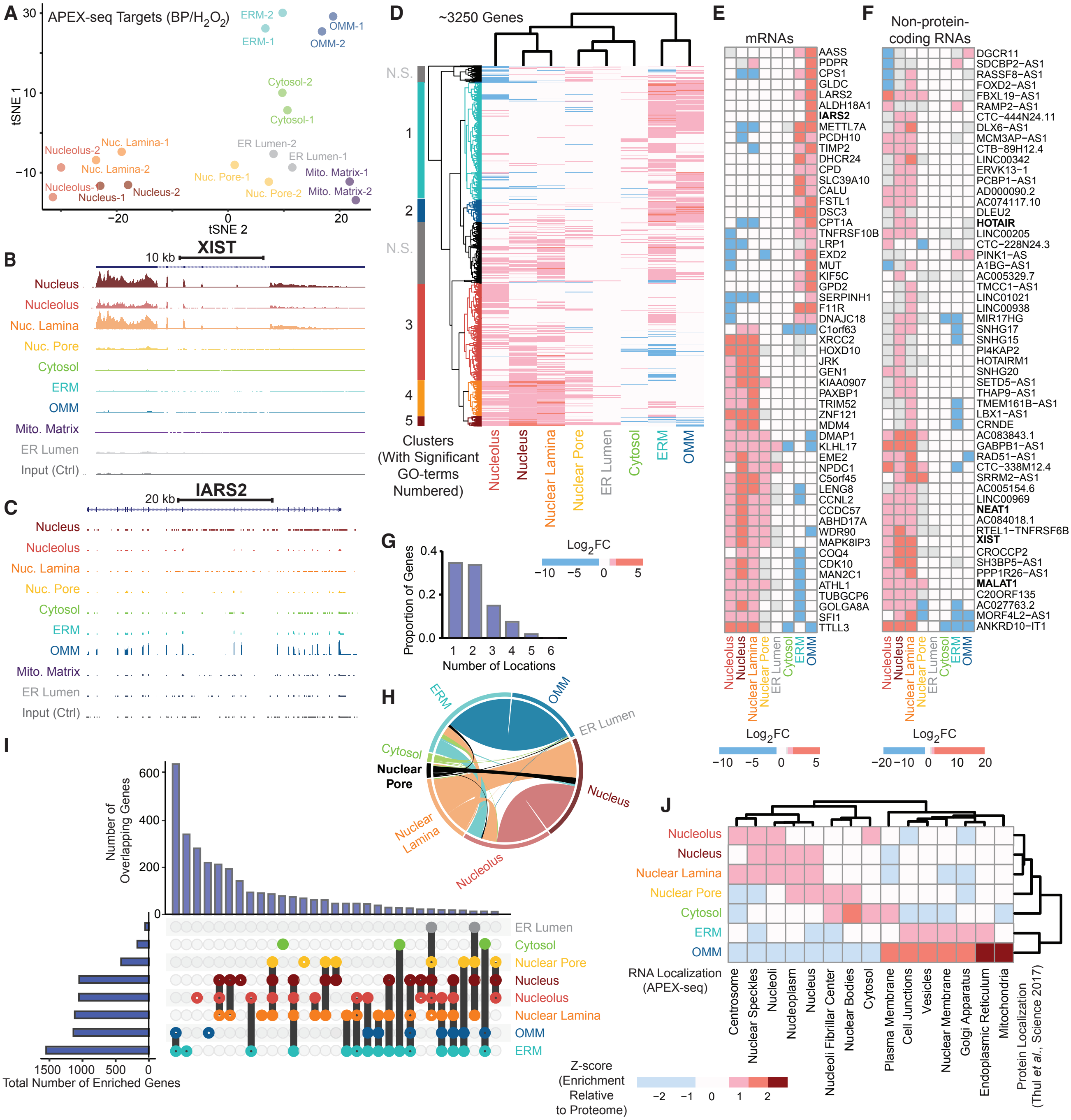

Figure 3. Analysis of Subcellular Transcriptome Maps

(A) T-distributed stochastic neighbor embedding (t-SNE) plot showing separation and clustering of APEX-seq libraries.

(B and C) Genome tracks for *XIST* (B), a nuclear non-coding RNA, and (C) *IARS2*, an mRNA encoding a mitochondrial tRNA synthetase. For each location, the reads were averaged across two APEX-seq replicates. The control tracks were generated by averaging 18 controls from all 9 constructs.

(D) Heatmap of transcripts enriched by APEX-seq showing clustering of the genes that specifically localize to at least one location and have fold-change data from all locations.

(E) Heatmap showing the APEX-seq fold changes for the mRNA transcripts found to be most variable among the locations investigated.

(F) Heatmap showing the APEX-seq fold changes for non-coding RNAs (excluding pseudogenes) that have the most-variable localization enrichment. A few well-known noncoding RNAs are shown in bold.

(G) Of the ~3,250 genes analyzed, most localize to only one or two of the eight locations (excluding mitochondrial matrix) interrogated.

(legend continued on next page)

they are impossible to purify and/or too small to image unambiguously by conventional microscopy. As such, it is impossible to generate true positive and false positive lists of known resident and non-resident RNAs respectively with which to perform ROC-based cutoff analysis. We therefore opted for a universal enrichment-factor cutoff of 0.75 ($\log_2$ fold change) and q value (false discovery rate [FDR]-adjusted p value) cutoff of 0.05, which was applied to all compartments (STAR Methods). By intersecting data from each pair of replicates, we obtained RNA lists for all nine compartments (Table S3).

These lists provide a wealth of observations about the RNA composition of diverse cellular locales. Many RNAs are "orphans," never previously linked to the compartment to which APEX-seq assigns them. For instance, our APEX-seq atlas (Figure 2F) newly assigns 324 RNAs to the nucleolus, 114 RNAs to the lamina, and 111 RNAs to the OMM. To provide further confidence in these spatial assignments, we analyzed a subset of high-abundance RNAs by sequential smFISH imaging (Figure 2I–2L) and found that 6 out of 10 OMM orphans and 7 out the 8 ERM orphans displayed significant smFISH enrichment at the mitochondria and ERM, respectively.

To further validate nuclear and cytosolic RNAs enriched by APEX-seq, we performed poly(A)+ nuclear/cytosolic fractionation of matched HEK cells (Figure 2G). Of the 95 nuclear and 14 cytosolic APEX-seq orphans for which we could obtain high-quality fractionation-seq reads, 84 of the nuclear and 4 of the cytosolic RNAs were validated (Figure 2F). Overall, fractionation-seq validated 81% (n = 88/109) of orphan genes.

The availability of matched fractionation-seq datasets gives us the opportunity to compare head-to-head with APEX-seq. Overall, we found that both nuclear and cytosolic APEX-seq datasets were much more specific than our corresponding fractionation-seq data. For instance, our APEX-seq gene lists lacked the mitochondrial matrix and ER contaminants present in the cytosolic and nuclear fractionation data, respectively (Figures 2G, 2H, and S3F). Excluding ER transcripts in the nuclear fractionation-seq dataset (using ERM APEX-seq gene list), we compared the remaining genes to APEX-seq in order to estimate the accuracy (94%) and precision (96%) of our methodology. We also observed that the RNA length distributions in nuclear fractionation and APEX-seq are very similar (Figure S3E).

General Features of the Human Transcriptome Revealed by APEX-Seq RNA Atlas

Our APEX-seq atlas reveals interesting patterns and features for the human transcriptome (Figure 3A). For >3,200 RNAs, we obtained high enrichment scores ($\log_2$ fold change >0.75) in at least one of the nine locations. Unbiased clustering analysis revealed that RNAs broadly partition into four general localization categories (Figures 3A and 3D): (1) nuclear, (2) mitochondrial membrane and ER, (3) cytosol, and (4) the remaining (which includes ER lumen, mitochondrial matrix, and nuclear pore). Most transcripts further localized to just one or two locations within each category (Figures 3D and 3G; STAR Methods). Comparing mRNAs to long noncoding RNAs (lncRNAs) (Figures 3E and 3F), our dataset showed that the former mostly localize to one of the cytosolic or nuclear locations, while lncRNAs are predominantly nuclear, consistent with previous studies (Cabili et al., 2015).

We observed substantial overlap between OMM and ERM-associated transcriptomes (Figures 3H and 3I). Using more stringent cutoffs based on ROC analysis, we confirmed that two-thirds of RNAs are shared by OMM and ERM, with almost 95% of shared mRNAs encoding secreted proteins (Figures S3C and S3D). It may be that specific subsets of mRNAs are translated at mitochondria-ER contact sites (Friedman et al., 2011; Giacomello and Pellegrini, 2016; Valm et al., 2017).

We used our APEX-seq atlas to explore the relationship between protein localization and localization of its encoding mRNA, making use of existing data on protein subcellular localization (Thul et al., 2017). Our analysis (Figure 3J) reveals remarkable concordance between RNA and protein localization at steady state. For example, the ERM-proximal transcriptome preferentially codes for proteins that localize to the ER, Golgi, and vesicles, rather than proteins that localize to the nucleus, nucleolus, or cytosol. Less expectedly, our data also show that mRNAs enriched in nuclear locations tend to code for proteins enriched in nuclear speckles and nucleoplasm, but not the plasma membrane (Figures 3J, S3A, and S3B). This result is surprising if protein translation occurs exclusively in the cytosol. Alternatively, it has been suggested that mRNAs in the nucleus might serve as "reserve pools" that help to dampen gene-expression noise (Bahar Halpern et al., 2015; Battich et al., 2015; Hansen et al., 2018). We speculate that nuclear-destined proteins (Thul et al., 2017), which are highly enriched for nucleic-acid binding proteins (FDR $< 5 \times 10^{-13}$, GO biological process) whose concentrations may have to be precisely tuned, may have mRNAs that are retained in nuclear subcompartments in order to better shield the amount of mRNA available for translation from noise.

The ability of our atlas to position endogenous RNAs with respect to distinct subcellular landmarks provides an exciting opportunity to test novel hypotheses concerning the relationship between RNA localization and function. For example, the atlas shows that *XIST* (X-inactive specific transcript), a nuclear lncRNA, is enriched at the nuclear lamina but not the nearby nuclear pore (Figure 3B). These findings are consistent with the known role of *XIST* in coating the inactive X chromosome in female cells (Penny et al., 1996), leading to transcriptional silencing and localization of the inactive X to the nuclear lamina (Chen et al., 2016). Another example is *IARS2* (mitochondrial isoleucyl tRNA synthetase 2, encoded by the nuclear genome), whose mRNA was identified by APEX-seq at the OMM (Figure 3C). Because *IARS2*'s protein product is known to reside in the mitochondrial matrix, the APEX-seq data suggest local translation of the mRNA at the OMM, a point we further explore in Figures 6 and 7.

Two other RNAs of note are *TUG1* and *NORAD*, lncRNAs localized by APEX-seq to both the ERM (validated by smFISH

(H) Circos plot showing the co-localization of RNAs to multiple locations.

(I) Transcripts overlapping in multiple locations.

(J) Heatmap showing the protein localization of the transcripts enriched by APEX-seq.

See also Figure S3.

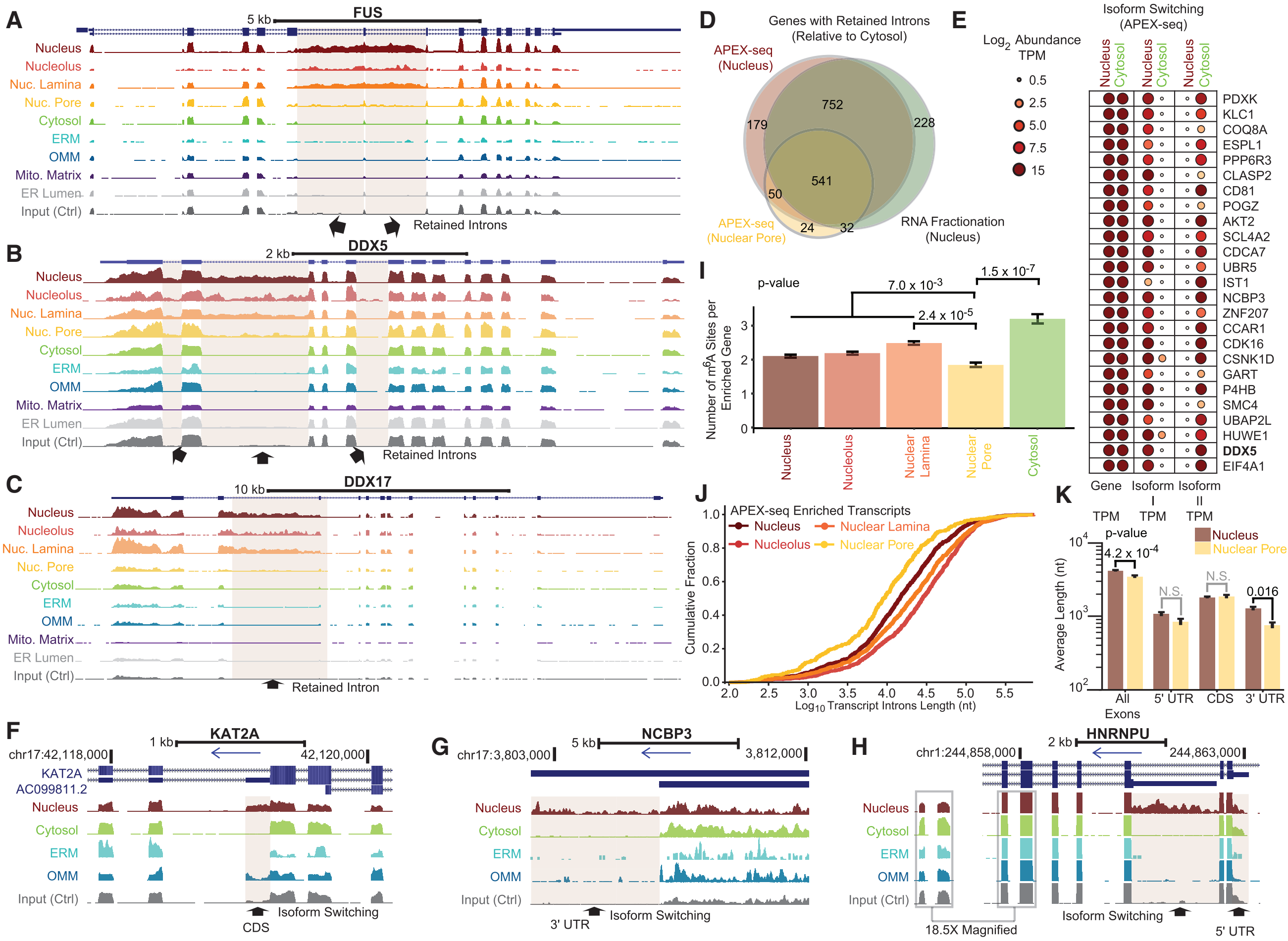

Figure 4. APEX-Seq Reveals Principles Related to RNA Isoforms and Introns

(A–C) The genome tracks of (A) *FUS* mRNA. (B) and (C) show the genome tracks of two other transcripts, *DDX5* and *DDX17*, with retained introns.

(D) Fractionation-seq (green) and nucleus APEX-seq (red) identify roughly the same genes with retained introns. The nuclear-pore APEX-seq transcriptome has fewer retained introns relative to the nucleus.

(E) Using APEX-seq, we identify transcripts that are highly abundant in both cytosol and nucleus at the gene level but switch isoforms at the transcript level. TPM, transcript per million.

(F–H) Browser tracks showing examples of isoform switching across nuclear and cytosolic locations for (F) *KAT2A* (lysine histone acetyltransferase 2A) in a putative coding sequence (CDS), (G) *NCBP3* (nuclear cap-binding protein subunit 3) in the 3′ UTR, and (H) *HNRNPU* (heterogenous nuclear ribonucleoprotein U) in the 5′ UTR, respectively. Arrows indicate direction of transcription.

(I) Number of m^{6}A present per transcript enriched by APEX-seq. High-confidence m^{6}A sites were obtained from the literature (Meyer et al., 2012). p values are from a Fisher's exact test.

(J) Cumulative distribution of the introns length for genes enriched by APEX-seq in the nuclear locations.

(K) Bar plots of average length of nuclear pore and nucleus enriched transcripts by mature transcript length, 5′ UTR, CDS (coding sequence) and 3′ UTR. p values are from a one-sided Mann-Whitney U test. Errors are SEM.

See also Figure S4.

imaging in Figures 2K and 2L) and the nucleus. While the majority (97%) of ERM APEX-seq-enriched species are mRNAs, our dataset highlights 31 noncoding RNAs, which are impossible to detect by ribosome profiling or ER fractionation-seq, because they are not translated.

APEX-Seq Reveals Differential Localization for Transcript Isoforms

Because APEX-seq is a sequencing-based methodology providing not only gene identity but full sequence details for each enriched RNA, we use it to support the hypothesis that different transcript isoforms of the same gene may localize to different regions of the cell (Mayr, 2017). For example, *FUS* (fused in sarcoma) mRNA, encoding a nuclear protein implicated in amyotrophic lateral sclerosis (ALS) and phase separation (Patel et al., 2015), shows intron retention within the nuclear locations, but not cytosolic ones (Figure 4A). Dead-BOX helicases 5 (*DDX5)* and 17 (*DDX17)* are additional examples of RNAs with retained introns (Figures 4B and 4C). The nuclear enrichment of retained introns was also observed in our fractionation-seq data

(r = 0.78) although without the sub-nuclear resolution that APEX-seq provides. Interestingly, we observed that APEX at the nuclear pore enriched fewer transcripts with retained introns than APEX at other nuclear locations (Figures 4D and S4A–S4C), consistent with the role of the pore as a ''gene gate'' for RNA quality control.

In addition to retained introns, APEX-seq revealed a group of RNAs that show no gene-level subcellular localization differences but exhibit substantial spatial heterogeneity at the transcript-isoform level (''isoform switching''; Figures 4E and S4A–S4E). Two such examples are the mRNAs for the oncogene *AKT2* and the circadian rhythm gene *CSNK1D*, which show isoform switching between the nucleus and cytosol. In some cases, isoform switching extends to the 5′ UTR, 3′ UTR, and coding regions of transcripts (Figures 4F–4H). Overall, we find hundreds of genes with alternative 5′ and 3′ splice sites (Figures S4F and S4G). These results naturally nominate specific exons associated with each isoform for localization to specific subcellular locations, which in turn could affect downstream functions (Berkovits and Mayr, 2015).

Nuclear Pore as a Staging Area for RNA Export

RNA transcripts must pass through the nuclear pore to go from their production sites in the nucleus into the cytoplasm. Previous studies have suggested that the nuclear pore may act as a staging area for cytoplasm-destined transcripts (Wickramasinghe and Laskey, 2015). Our APEX-seq data reveal a striking similarity between RNAs enriched at the nuclear face of the nuclear pore (where APEX is expressed as a fusion to the pore-basket-binder SENP2 (Sentrin-specific protease 2) (Walther et al., 2001) and RNAs in the cytoplasm (Figure 3D), in contrast to RNAs from other nuclear locations (Figure 3A).

Our results support the prevailing view that the nucleoplasmic milieu (Blobel, 1985; Brown and Silver, 2007; Kim et al., 2018) of the pore has a critical role in mRNA surveillance, allowing only properly spliced and sorted transcripts ready for export to cytoplasm to congregate (while retaining partially spliced transcripts in the nucleus) (Figures 4A–4C).

m^{6}A Modification and RNA Length in Nuclear Pore Localization

While RNA processing for nuclear export is complex and highly regulated, the rate-limiting step for mRNA transport is believed to be access to and release from the nuclear pore complex (NPC) (Grünwald and Singer, 2010; Ma et al., 2013). *N6*-methyladenosine (m^{6}A) modification of pre-messenger RNAs has been reported as a ''fast track'' signal for nuclear export (Roundtree et al., 2017), while RNA length has been hypothesized as a feature influencing RNA export, with long RNAs taking more time to remodel and exit.

When we intersected nuclear-pore APEX-seq data with m^{6}A modification sites (Meyer et al., 2012), we found a significant depletion of m^{6}A in transcripts enriched near the pore, compared to nuclear lamina or the cytosol (Figure 4I). Our data support the hypothesis that m^{6}A-modified transcripts transit quickly through the NPC, leading to low biotinylation by APEX-seq. However, although transcripts at the pore had less m^{6}A than other nuclear locations, the transcript density of m^{6}A was not significantly different across these locations. Nonetheless, transcripts at both the pore and other nuclear locations had lower m^{6}A density (i.e., sites per kilobase) than the cytosol.

We also examined RNA length in our nuclear-pore APEX-seq data. We found that transcripts enriched at the pore tend to be shorter than transcripts at other nuclear locations. This inverse relationship between RNA length and nuclear pore APEX enrichment is significant both in the mature transcript and the introns only (Figures 4J, 4K, S4H, and S4K). For protein-coding transcripts, the 3′-UTR length is most predictive of nuclear pore APEX-seq enrichment (Figure 4K). A possible interpretation of our data is that longer RNAs pass more quickly through the pore, leading to lower APEX-seq enrichment, which could be the case if shorter RNAs assemble with fewer RNA-binding proteins (RBPs), including those necessary for recognition and passage through the pore.

Although different processes exist to export intronless mRNAs (Delaleau and Borden, 2015), we did not observe a significant difference in the proportion of intronless transcripts at the pore relative to other locations (Figure S4I).

RNA Repeats and Genomic Position Influence Sub-Nuclear RNA Localization

Repeat sequences make up a majority of the human genome (de Koning et al., 2011), with interspersed nuclear elements SINE (short) and LINE (long) containing retrotransposable (transposable via RNA intermediates) elements that can be deleterious when active and randomly moving to new genomic sites (Ichiyanagi, 2013). We observed enrichment of SINEs and LINEs within the nuclear locations (Figures 5A and S5A–S5D), with the highest enrichment of these elements in the nuclear lamina. The cytosolic locations and the nuclear pore showed no enrichment (Figure S5E). Given the known accumulation of transcription-repression machinery at the lamina (van Steensel and Belmont, 2017), our observations may help to explain the recent findings that LINE (L1) elements are epigenetically silenced (Padeken et al., 2015). Likewise, transcripts enriched at the nuclear lamina had lower expression level than other nuclear locations, consistent with the idea of heterochromatin deposition and gene silencing at lamina-associated domains (LADs) (Figures 5C and S5G–S5I).

Second, location of the DNA locus from which an RNA originates is believed to strongly dictate nuclear RNA location (Dekker et al., 2017), which we find support for. For example, previous work has shown that the nucleolus is enriched for DNA coding for rRNAs (van Koningsbruggen et al., 2010), while our APEX-seq atlas shows that rRNA repeat motifs (Wheeler et al., 2013) are highly enriched in the nucleolus but far less in the nuclear lamina or cytosol (Figure 5B). We also find that mRNA of genes residing in DNA nucleolus-associated domains (NADs) (Dillinger et al., 2017; van Koningsbruggen et al., 2010) are highly enriched in the nucleolus (odds ratio = 4.4; 95% confidence interval [CI] = 1.7–14) (Figures 5D and S5J). For DNA loci in LADs (Guelen et al., 2008), their corresponding RNA were enriched in the lamina APEX-seq (odds ratio = 11; 95% CI = 3.8–43) (Figures S5J–S5M).

Distinct Mechanisms of mRNA Localization to the OMM

Human mitochondrion contains >1,100 protein species (Calvo et al., 2016), only 13 of which are encoded by the mitochondrial

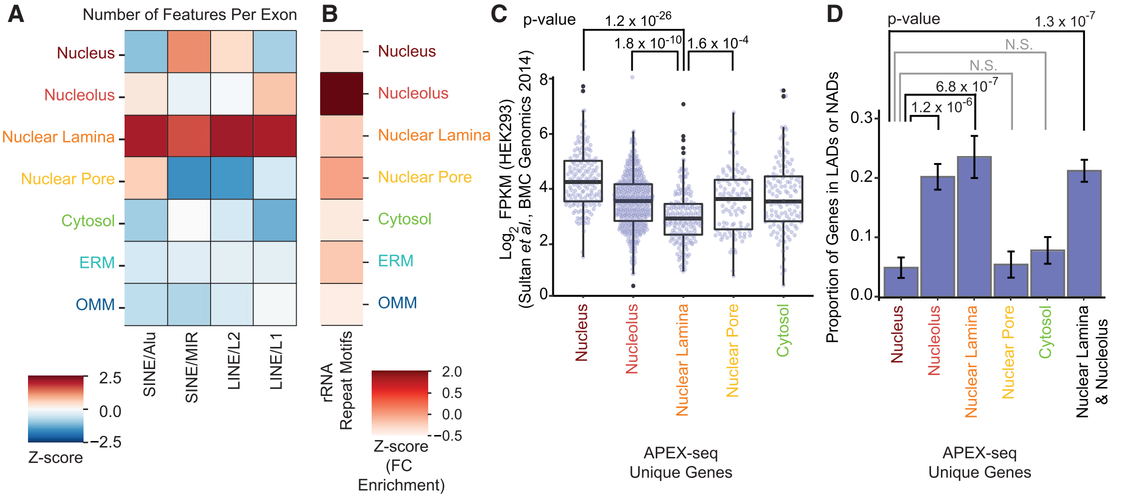

Figure 5. The Underlying Features of Nuclear RNA Localization

(A) Examination of retrotransposable elements in transcripts uniquely localizing to different locations show an enrichment of these elements in the nuclear-lamina transcriptome.

(B) Heatmap of *Z* score showing that transcripts localizing to the nucleolus are enriched in rRNA repeat motifs, relative to the nucleus.

(C) Within the nuclear locations, the nuclear-lamina-enriched transcripts have a lower abundance relative to both the nucleus and the nucleolus. p value is from a Mann-Whitney U test.

(D) Examination of the genes found in DNA lamina-associated domains (LADs) and nucleolus-associated domains (NADs) confirms that the corresponding transcriptomes are enriched for those genes. Here we restrict analysis to transcripts uniquely enriched in the respective locations. p values are from Fisher's exact tests.

See also Figure S5.

genome (mtDNA) and translated within the organelle. The remainder are encoded by the nuclear genome and must be delivered to the mitochondrion after translation in the cytosol (Mercer et al., 2011). The identification of ribosomes at the OMM (Kellems et al., 1974, 1975) led to the hypothesis that some mRNAs encoding mitochondrial proteins may be locally translated at the OMM and co-translationally or post-translationally imported into the mitochondrion (Gold et al., 2017) (Figure 6A). However, at present little is known about the landscape of RNAs at the mammalian mitochondrial membrane, despite its importance for understanding mitochondrial biogenesis.

We mined our APEX-seq atlas for insights about mitochondria-proximal RNAs in human cells and found that the OMM compartment was enriched in mRNAs encoding mitochondrial proteins (Figure 3J). When plotted by OMM APEX-seq enrichment, we observed a significant increase in enrichment of nuclear-encoded mitochondrial genes over non-mitochondrial, non-secretory genes (Figure 6B; Table S4). By contrast, no increase in enrichment of mitochondrial genes was observed when RNAs were plotted by ERM APEX-seq enrichment score (Figure 6C). These results support the notion that mitochondrial transcripts accumulate at the OMM, possibly for the purpose of local protein translation. Examination of our OMM-enriched mRNAs did not reveal any pattern in terms of protein functional class or sub-mitochondrial localization of the encoded proteins. In an effort to further tease apart possible mRNA subpopulations that may be targeted to the OMM by different mechanisms, we repeated APEX-seq labeling under different perturbation conditions.

Taking advantage of the rapidity of APEX-seq tagging, we treated cells expressing OMM-APEX2 with cycloheximide (CHX), puromycin (PUR), or carbonyl cyanide m-chlorophenyl hydrazone (CCCP), prior to labeling (Figure S6A). CHX and PUR are both protein translation inhibitors but they work by different mechanisms. CHX stalls translation but preserves the mRNA-ribosome-nascent protein chain complex, while PUR dissociates mRNAs from ribosomes. CCCP abolishes the mitochondrial membrane potential and thereby stops membrane potential-dependent processes including TOM (translocase of outer membrane)/TIM-mediated import of mitochondrial proteins (Chacinska et al., 2009).

After treatment of cells with CHX, we observed a dramatic increase in the number of mitochondrial genes and their extent of OMM enrichment (Figures 6B and 6D), consistent with a model in which mRNA localization to the OMM can be regulated by the encoded protein's mitochondria-targeting sequence. As it emerges from the ribosome, the nascent peptide is localized to the OMM together with the still translating mRNA. Indeed, we found that the most-CHX-enriched mitochondrial genes have higher TargetP scores on average (Figures 6E–6G); TargetP is a measure of mitochondrial targeting potential (Emanuelsson et al., 2007). Hence, OMM APEX-seq following CHX appears to highlight a subpopulation of that may localize to the OMM in a ribosome-dependent fashion (Figure 6H). Figures 6I and S6C show the genome tracks of example mRNAs, *HSPA9* (mitochondria heat shock protein A9) and *MUT* (methylmalonyl-coA mutase), respectively, that display increased OMM localization upon CHX treatment.

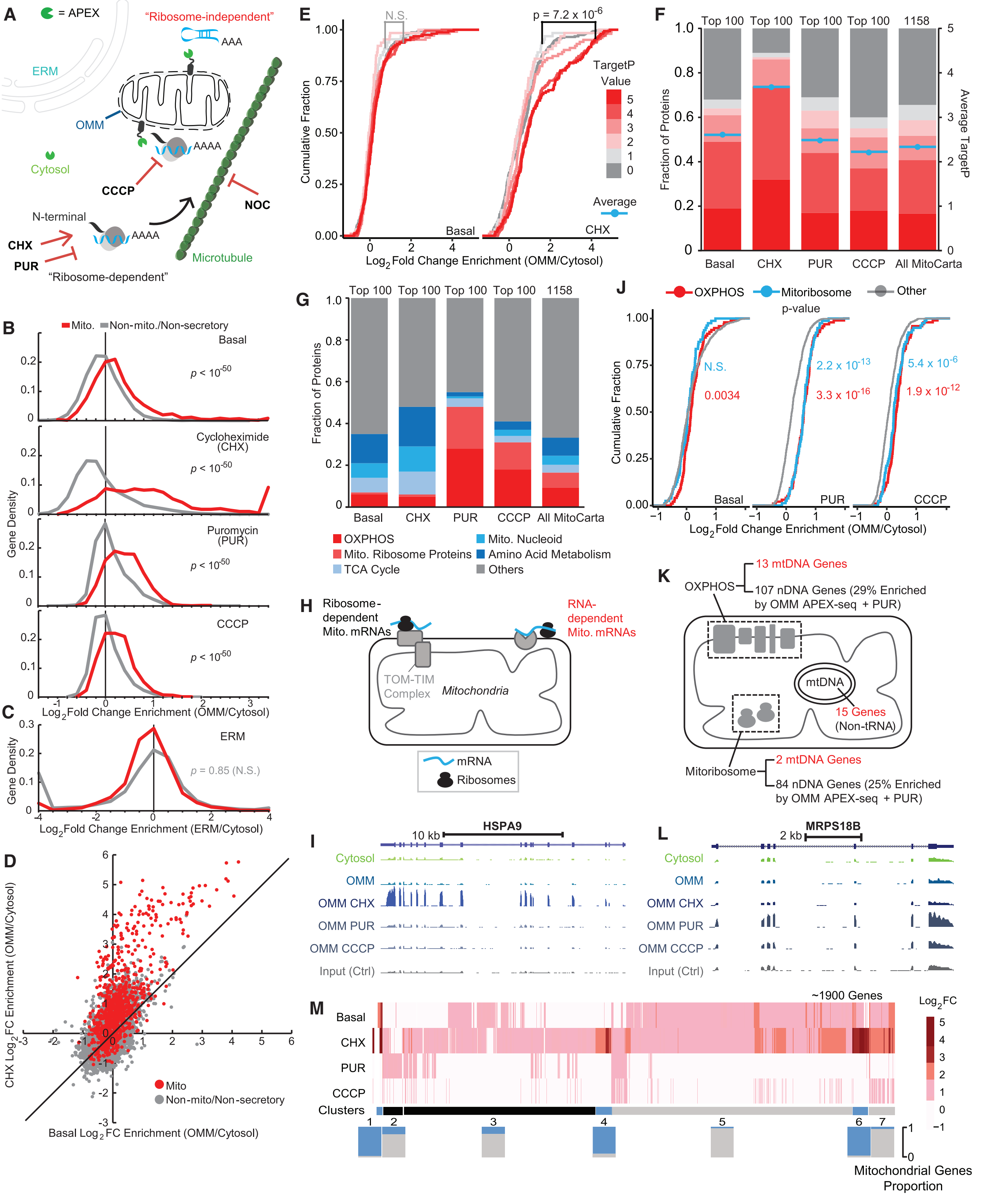

(legend on next page)

Treatment of cells with PUR produced a pattern of enrichment distinct from CHX treatment. The vast majority of CHX-enriched mRNAs were no longer observed at the OMM, consistent with the hypothesis that the localization of these transcripts depends on an intact ribosome complex (Figures 6B and S6E). Nonetheless, a subpopulation of mRNAs remained clearly associated with the OMM after PUR; the top OMM-localized genes were not higher in TargetP, in contrast to CHX-enriched genes (Figure 6F). Functional class analysis revealed that PUR-enriched genes have a higher likelihood of encoding mitochondrial ribosome and oxidative phosphorylation (OXPHOS) components (Figures 6G, 6J, 6K, and S6F), which are the two complexes that require the coordinated assembly from the nuclear and mitochondrial genomes (Couvillion et al., 2016). Figures 6L and S6D show genome tracks of a representative mitochondrial ribosomal-protein gene, *MRPS18B* (28S ribosomal protein S18b), and OXPHOS gene, *NDUFB9* (NADH:ubiquinone oxidoreductase subunit B9), respectively. The PUR data thus suggest that a subpopulation of mRNAs associates with the OMM in a ribosome- and nascent-chain-independent fashion, perhaps by binding directly to a OMM-localized RNA binding protein (Figure 6H).

Upon treatment with the mitochondrial uncoupler CCCP, the genes enriched at the OMM are similar to PUR-enriched genes (Figures 6F, 6G, and 6J). CCCP-enriched genes must not depend on the mitochondrial membrane potential or mitochondrial protein import for their OMM localization. Perhaps by causing a reduction in interactions between the ribosome-mRNA-nascent chain complexes and TOM/TIM at the OMM, the association of ribosome-*independent* mRNAs with the OMM under CCCP becomes more readily apparent.

The availability of basal along with three "drug perturbation" OMM APEX-seq datasets enabled us to perform higher-order clustering analysis. Figure 6M shows transcripts that were enriched at the OMM in at least one condition. We find that RNAs cluster into groups based on their enrichment in CHX versus PUR, with some clusters strongly predictive of genes coding for mitochondrial proteins (Figure S6H). In particular, in clusters 1, 4, and 6 that included transcripts strongly enriched upon CHX treatment and depleted upon PUR treatment, >90% of RNAs (n = 128/140) code for mitochondrial proteins. 7 of the remaining 12 transcripts were pseudogenes, with at least 3 of the 5 mRNAs likely to be mitochondrial (Figures S6I–S6J) based on other studies (Mou et al., 2009; Pandey et al., 2017; Thul et al., 2017). Thus, OMM APEX-seq data could be used to predict whether certain genes will code for mitochondrial proteins.

Analysis of Motifs that Predict RNA Localization to the Mitochondrion

By using PUR and CHX treatments, we disentangled RNA populations that localize to the OMM via ribosome-dependent versus ribosome-independent mechanisms (Figure 6H). We next investigated two hypotheses: (1) that PUR-enriched mRNAs ("ribosome-independent") possess specific RNA sequences that predict their OMM localization, and (2) that CHX-enriched mRNAs ("ribosome-dependent") possess specific amino-acid features that predict OMM localization. To test these hypotheses, we first classified OMM-enriched transcripts as either ribosome-dependent or RNA dependent (if they localized to OMM under PUR) (Figure 7A). We trained a random-forest classification algorithm to predict localization of these two categories of transcripts to the OMM versus the ERM (which we used as "background"), using 6-mers as RNA features (STAR Methods). The resulting classifier was much better at predicting localization of RNA-dependent transcripts relative to ribosome-dependent ones (Figure 7B). The converse result was obtained when using the corresponding N-terminal 100 amino acid peptide for training (Figures 7C and 7D), suggesting that the peptide sequence is more predictive for ribosome-dependent transcripts.

We looked further into the RNA features that may be predictive of OMM localization (Table S5) and found that the 5′ UTR was least important and the 3′ UTR most informative (Figures S7A and S7B). The most-important 6-mer sequences were G/U rich, with one of the other top hits being the poly(A)-signal

Figure 6. Distinct Subpopulations of mRNAs at the OMM

(A) Schematic diagram showing the mitochondria with all perturbations used in this study, including those that affect ribosomes (puromycin [PUR] and cycloheximide [CHX]), mitochondrial membrane potential (carbonyl cyanide m-chlorophenyl hydrazone [CCCP]), and microtubules (nocodazole [NOC]). RNA is shown in blue, ribosomes in gray, and microtubules in green.

(B) Gene density distribution of OMM APEX-seq enrichment under different conditions. p values are from Mann-Whitney U tests.

(C) Gene density distribution of ERM APEX-seq enrichment. Genes are categorized as in (B). p value is from a Mann-Whitney U test.

(D) Scatterplot of OMM APEX-seq $\log_2$ fold change comparing the basal and CHX conditions.

(E) Cumulative fraction of genes in different conditions by TargetP values. CHX treatment shows increased OMM targeting of genes with high TargetP values. Genes are categorized by their TargetP values (see STAR Methods) on a scale from 5 (strongest N-terminal mitochondrial targeting peptide) to 0 (no N-terminal mitochondrial targeting peptide). p values are from Kolmogorov-Smirnov (KS) test.

(F) Comparing the proportion of transcripts with different TargetP values and average TargetP value among top 100 mitochondrial genes enriched by OMM APEX-seq in cells under different conditions and all MitoCarta genes.

(G) Comparing the proportion of transcripts in different functional classes among top 100 mitochondrial genes enriched by OMM APEX-seq in cells under different conditions and all MitoCarta genes. Genes are functionally classified according to Gene Ontology.

(H) Model summarizing two distinct subpopulations of mitochondrial RNAs proximal to mitochondria.

(I) Browser tracks of a mitochondrial gene (*HSPA9*, targetP = 5) show increased enrichment by OMM-APEX upon CHX treatment.

(J) Cumulative fraction of OXPHOS and mitoribosome-related genes in different conditions. p values are from KS test.

(K) Scheme illustrating the coordinated assembly of respiratory chain complexes and mitoribosomes between the nuclear and mitochondrial genomes.

(L) Browser tracks of a mitochondrial ribosomal gene (*MRPS18B*) that show increased enrichment by OMM-APEX upon PUR or CCCP treatment.

(M) Heatmap of fold changes for transcripts enriched by OMM APEX-seq. Upon clustering based on the basal, CHX, and PUR conditions, we obtain clusters that are either strongly enriched or depleted in the corresponding mitochondrial proteins.

See also Figure S6 and Table S4.

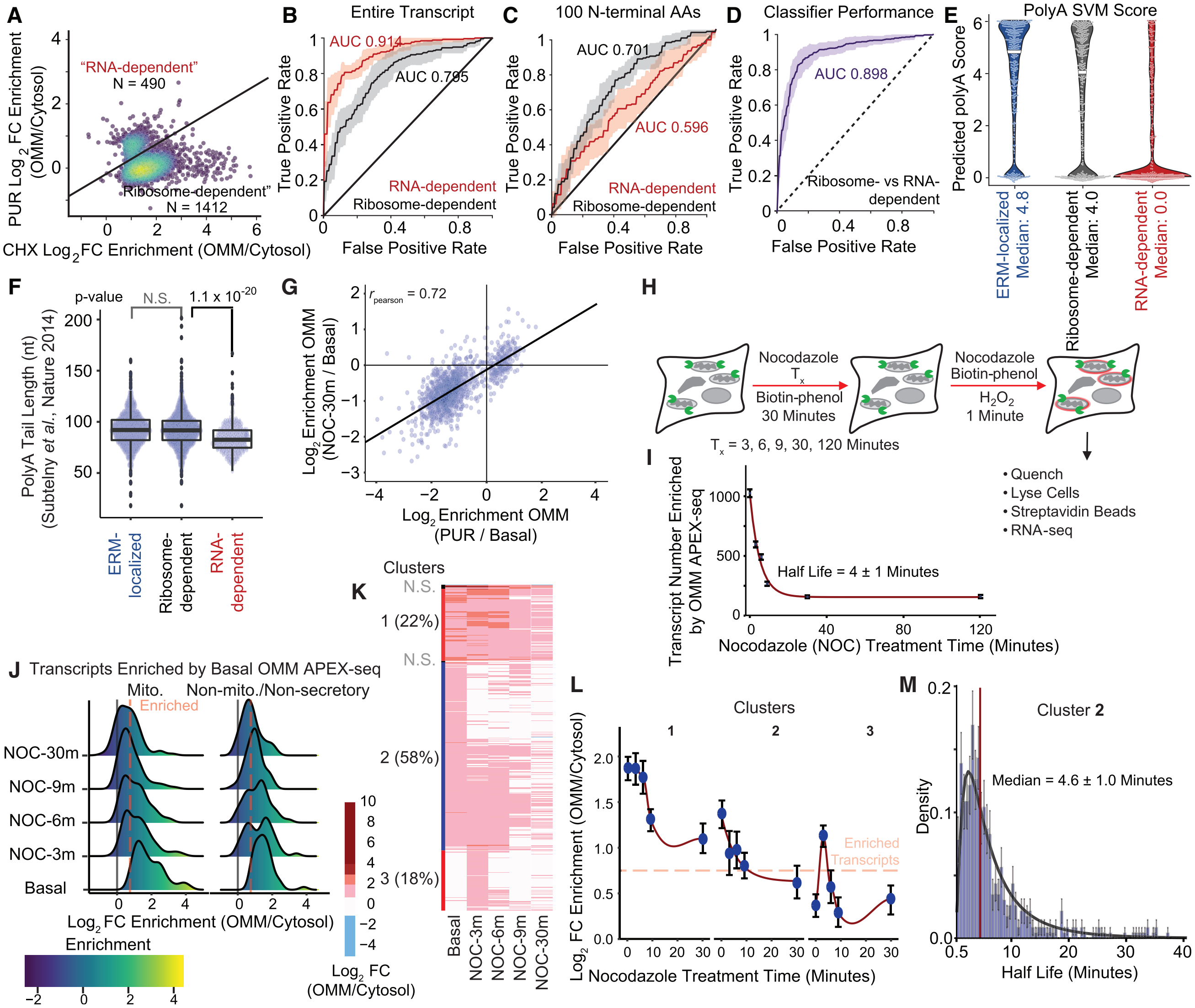

Figure 7. Features of Ribosome-Dependent and RNA-Dependent Transcripts at OMM

(A) Based on the effect of PUR and CHX, we binned genes from heatmap (Figure 6M) into two categories: ribosome dependent and RNA dependent.

(B) ROC curves from an unsupervised random-forest classifier that predicts transcript localization to OMM (versus ERM). To train the classifier, the transcript sequences were divided into 4,096 (= 4^6) 6-mers. Plotted is the mean performance (dark line) and the range from 10-fold cross-validation.

(C) Same as (B) but using the first 100 coding amino acids (aa) for training. Due to the much larger possible space of aa-variation, we used 3-mers (= 22^3 k-mers) instead of 6-mers for training.

(D) Similar model using 6-mer RNA sequences was used to classify transcripts as ribosome-dependent or RNA-dependent.

(E) Using the poly(A) SVM package, which predicts polyadenylation site scores, we find the RNA-dependent transcripts have low polyadenylation scores.

(F) Using a poly(A) tail-length dataset (Subtelny et al., 2014), we found RNA-dependent transcripts have shorter poly(A)-tail length relative to ribosome-dependent transcripts. p values are from Mann-Whitney U test.

(G) Correlation of fold change upon 30-min NOC treatment (where effect saturates) and the corresponding change upon PUR treatment. Changes are measured relative to basal conditions.

(H) Schematic diagram of the time-course APEX-seq protocol.

(I) Number of transcripts enriched by OMM-APEX-seq.

(J) Progressive depletion of basal OMM transcripts upon NOC treatment.

(K) Heatmap of genes enriched by APEX-seq in any of the time points. We clustered on the first 4 times points.

(L) Enrichment change as function of NOC treatment time for the three major clusters. Data are median fold change ±1 sigma.

(M) Half-lives for transcripts in Cluster 2.

See also Figure S7 and Tables S5 and S6.

sequence AAUAAA (Figure S7C). In support of our findings, the predicted poly(A) SVM score (a measure of poly(A)-site prediction) (Cheng et al., 2006) of RNA-dependent transcripts is substantially different from that of ribosome-dependent transcripts (Figure 7E). We also found that RNA-dependent OMM transcripts have significantly shorter poly(A)-tail lengths than ribosome-dependent transcripts, as well as shorter 3′ UTRs (Figures 7F and S7D). Altogether, our findings support the two hypotheses above and reveal specific RNA and protein features that are predictive of OMM localization.

Kinetics of RNA Transport to the Mitochondrion

Previous studies have suggested that RNA may arrive at the OMM via active microtubule-based transport (Buxbaum et al., 2015). To investigate this hypothesis, we repeated the OMM APEX-seq labeling after treating cells for various lengths of time with the microtubule-polymerization inhibitor nocodazole (NOC), which is known to inhibit transport (Reck-Peterson et al., 2018; Shen et al., 2018). We confirmed by imaging that NOC treatment does not perturb the localization of the OMM-APEX2 construct (Figure S7E). Figures 7H and 7I shows that 30 min of NOC led to a depletion of mRNAs at the OMM. The RNAs remaining at the OMM were more similar to those observed under PUR ($r = 0.72$) compared to those under CHX ($r = 0.32$) (Figures 7G and S7H). The selective disappearance of ribosome-dependent mRNAs from the OMM suggests that these mRNAs may utilize the cytoskeletal network to reach the OMM (Figure 6A).

Analysis of NOC time-course data (Figures 7H, 7I, S7F, and S7G; Table S6) showed that the majority of RNAs disappear rapidly from the OMM following NOC treatment. This decrease is observed for both mRNAs that encode mitochondrial proteins and other RNAs (Figure 7J). Further analysis resolved at least three patterns of responses to NOC (Figures 7K and 7L). The largest cluster shows rapid loss from the OMM with half-life dissociation data that could be fit by a log-normal distribution (Figure 7M), suggesting that many rate-limiting events could be involved. While further studies are needed to characterize these responses (as perturbing the cytoskeleton can have wide-ranging effects), our observations do showcase the power of rapid APEX-seq labeling to resolve dynamic transcriptome-wide RNA localization events.

DISCUSSION

With quantitative enrichment scores and detailed transcript profiles for over 25,000 distinct human RNA species across nine subcellular compartments, our study reveals patterns of RNA localization that give rise to a variety of biological hypotheses. APEX-seq yields RNA sequence information down to single-nucleotide resolution, thereby filling a critical gap in the landscape of RNA technologies. Our APEX-seq-derived atlas of transcriptome localization provides a comprehensive and precise delineation of RNA spatial organization in the living cell.

APEX-seq adds to arsenal of RNA localization methods while offering unique advantages. The first strength of APEX-seq is that labeling is performed in living cells, while membranes and macromolecular complexes are still intact. Second, APEX-seq can be used to analyze “unpurifiable” structures such as the nuclear lamina and OMM that are impossible to access via fractionation-based approaches. The third strength of APEX-seq is that it provides full sequence information for diverse classes of RNA transcripts, allowing transcript isoforms with distinct localization to be distinguished (Figures 4F–4H). Fourth, while ribosome profiling captures actively translating mRNA on polysomes, APEX-seq additionally detects lncRNAs, antisense RNAs (Figures 3E and 3F) and untranslated mRNAs not bound to ribosomes. Finally, the high spatiotemporal resolution sets APEX-seq apart from APEX-RIP, which loses spatial specificity in non-membrane enclosed regions (Figure 1D).

A disadvantage of APEX-seq is that it requires an APEX fusion construct to be recombinantly expressed in the cell of interest, which limits applicability to human tissue. Also, APEX-seq does not provide single-cell information like imaging-based methods. Finally, because labeling is performed in live cells, APEX-seq coverage will be fundamentally limited by the steric accessibility of RNAs in their native environment; RNAs that are buried within macromolecular complexes may not be tagged. These limitations suggest directions for future improvement.

We expect that APEX-seq will be broadly applicable to many organisms and cell types, just as APEX proteomics has been extended to flies (Chen et al., 2015a), worms (Reinke et al., 2017), yeast (Hwang and Espenshade, 2016), and neurons (Loh et al., 2016). APEX-seq could be fruitfully applied to polarized cells, neurons, or dynamic developmental systems. Future use of APEX-seq in conjunction with RNA-structure-mapping methods (Chin and Lécuyer, 2017; Spitale et al., 2015; Sun et al., 2019), RBP-occupancy atlases (Van Nostrand et al., 2016), and massively parallel reporter gene assays (Lubelsky and Ulitsky, 2018; Shukla et al., 2018) could shed light on the molecular basis of the spatial organization of RNA within cells.

STAR★METHODS

Detailed methods are provided in the online version of this paper and include the following:

- KEY RESOURCES TABLE
- LEAD CONTACT AND MATERIALS AVAILABILITY
- EXPERIMENTAL MODEL AND SUBJECT DETAILS
  - ○ Mammalian cell culture
  - ○ Generation of HEK293T cells stably expressing different APEX2 constructs
- METHOD DETAILS
  - ○ APEX labeling in living cells
  - ○ Immunofluorescence staining and fluorescence microscopy
  - ○ RNA extraction for RT-qPCR or RNA-seq
  - ○ APEX labeling streptavidin dot blot experiment
  - ○ Horseradish peroxidase (HRP) *in vitro* labeling
  - ○ Enrichment of biotinylated RNA
  - ○ APEX-seq library preparation

SUPPLEMENTAL INFORMATION

Supplemental Information can be found online at https://doi.org/10.1016/j.cell.2019.05.027.

ACKNOWLEDGMENTS

We thank members of the Ting and Chang labs for analysis suggestions and critical reading of the manuscript, J. Coller and X. Ji for sequencing, and L. Mateo for assistance with microscopy. This work was supported by NIH (R01-CA186568-1 to A.Y.T.; R01-HG004361 and P50-HG007735 to H.Y.C.; S10OD018220 to Stanford Functional Genomics Facility), Burroughs Wellcome (CASI grant to A.N.B.), and the Chan Zuckerberg Biohub (to A.Y.T.). F.M.F. was supported by the NIH T32 SGTP and the Arnold. O. Beckman Postdoctoral Fellowships. S.H. was supported by the Stanford Bio-X Bowes Fellowship. H.Y.C. is an Investigator of HHMI. A.Y.T. is a Chan Zuckerberg Biohub Investigator.

AUTHOR CONTRIBUTIONS

F.M.F., P.K., H.Y.C., and A.Y.T. conceived the project. F.M.F., S.H., P.K., H.Y.C., and A.Y.T. designed experiments. F.M.F., S.H., and P.K. performed all experiments, unless otherwise noted. F.M.F. designed and carried out sequencing experiments. S.H., A.N.B., and A.Y.T. designed and carried out sequential FISH experiments. F.M.F., S.H., K.R.P., P.K., J.X., and A.Y.T. analyzed data. F.M.F., S.H., H.Y.C., and A.Y.T. wrote the paper with input from all authors. H.Y.C. and A.Y.T. jointly supervised work and acquired funding.

DECLARATION OF INTERESTS

A.Y.T., P.K., H.Y.C., and F.M.F. have filed a patent application covering aspects of this work (Patent Application Number US 2017/0226561). H.Y.C. is a co-founder and advisor of Accent Therapeutics. H.Y.C. is an advisor of 10X Genomics and Spring Discovery.

Received: August 31, 2018
Revised: December 31, 2018
Accepted: May 14, 2019
Published: June 20, 2019

REFERENCES

Anders, S., Reyes, A., and Huber, W. (2012). Detecting differential usage of exons from RNA-seq data. Genome Res. *22*, 2008–2017.

Anders, S., Pyl, P.T., and Huber, W. (2014). HTSeq - A Python Framework to Work with High-Throughput Sequencing Data (Cold Spring Harbor Laboratory).

Bahar Halpern, K., Caspi, I., Lemze, D., Levy, M., Landen, S., Elinav, E., Ulitsky, I., and Itzkovitz, S. (2015). Nuclear Retention of mRNA in Mammalian Tissues. Cell Rep. *13*, 2653–2662.

Battich, N., Stoeger, T., and Pelkmans, L. (2015). Control of transcript variability in single mammalian cells. Cell *163*, 1596–1610.

Benhalevy, D., Anastasakis, D.G., and Hafner, M. (2018). Proximity-CLIP provides a snapshot of protein-occupied RNA elements in subcellular compartments. Nat. Methods *15*, 1074–1082.

Berkovits, B.D., and Mayr, C. (2015). Alternative 3′ UTRs act as scaffolds to regulate membrane protein localization. Nature *522*, 363–367.

Bertrand, E., Chartrand, P., Schaefer, M., Shenoy, S.M., Singer, R.H., and Long, R.M. (1998). Localization of ASH1 mRNA particles in living yeast. Mol. Cell *2*, 437–445.

Blobel, G. (1985). Gene gating: a hypothesis. Proc. Natl. Acad. Sci. USA *82*, 8527–8529.

Bolger, A.M., Lohse, M., and Usadel, B. (2014). Trimmomatic: a flexible trimmer for Illumina sequence data. Bioinformatics *30*, 2114–2120.

Bray, N.L., Pimentel, H., Melsted, P., and Pachter, L. (2016). Near-optimal probabilistic RNA-seq quantification. Nat. Biotechnol. *34*, 525–527.

Brown, C.R., and Silver, P.A. (2007). Transcriptional regulation at the nuclear pore complex. Curr. Opin. Genet. Dev. *17*, 100–106.

Buxbaum, A.R., Haimovich, G., and Singer, R.H. (2015). In the right place at the right time: visualizing and understanding mRNA localization. Nat. Rev. Mol. Cell Biol. *16*, 95–109.

Cabili, M.N., Dunagin, M.C., McClanahan, P.D., Biaesch, A., Padovan-Merhar, O., Regev, A., Rinn, J.L., and Raj, A. (2015). Localization and abundance analysis of human lncRNAs at single-cell and single-molecule resolution. Genome Biol. *16*, 20.

Calvo, S.E., Clauser, K.R., and Mootha, V.K. (2016). MitoCarta2.0: an updated inventory of mammalian mitochondrial proteins. Nucleic Acids Res. *44* (D1), D1251–D1257.

Chacinska, A., Koehler, C.M., Milenkovic, D., Lithgow, T., and Pfanner, N. (2009). Importing mitochondrial proteins: machineries and mechanisms. Cell *138*, 628–644.

Chen, C.L., Hu, Y., Udeshi, N.D., Lau, T.Y., Wirtz-Peitz, F., He, L., Ting, A.Y., Carr, S.A., and Perrimon, N. (2015a). Proteomic mapping in live Drosophila tissues using an engineered ascorbate peroxidase. Proc. Natl. Acad. Sci. USA *112*, 12093–12098.

Chen, K.H., Boettiger, A.N., Moffitt, J.R., Wang, S., and Zhuang, X. (2015b). RNA imaging. Spatially resolved, highly multiplexed RNA profiling in single cells. Science *348*, aaa6090.

Chen, C.K., Blanco, M., Jackson, C., Aznauryan, E., Ollikainen, N., Surka, C., Chow, A., Cerase, A., McDonel, P., and Guttman, M. (2016). Xist recruits the X chromosome to the nuclear lamina to enable chromosome-wide silencing. Science *354*, 468–472.

Cheng, Y., Miura, R.M., and Tian, B. (2006). Prediction of mRNA polyadenylation sites by support vector machine. Bioinformatics *22*, 2320–2325.

Chin, A., and Lécuyer, E. (2017). RNA localization: Making its way to the center stage. Biochim. Biophys. Acta, Gen. Subj. *1861* (11 Pt B), 2956–2970.

Couvillion, M.T., Soto, I.C., Shipkovenska, G., and Churchman, L.S. (2016). Synchronized mitochondrial and cytosolic translation programs. Nature *533*, 499–503.

de Koning, A.P., Gu, W., Castoe, T.A., Batzer, M.A., and Pollock, D.D. (2011). Repetitive elements may comprise over two-thirds of the human genome. PLoS Genet. *7*, e1002384.

Dekker, J., Belmont, A.S., Guttman, M., Leshyk, V.O., Lis, J.T., Lomvardas, S., Mirny, L.A., O'Shea, C.C., Park, P.J., Ren, B., et al.; 4D Nucleome Network (2017). The 4D nucleome project. Nature *549*, 219–226.

Delaleau, M., and Borden, K.L. (2015). Multiple export mechanisms for mRNAs. Cells *4*, 452–473.

Dillinger, S., Straub, T., and Németh, A. (2017). Nucleolus association of chromosomal domains is largely maintained in cellular senescence despite massive nuclear reorganisation. PLoS ONE *12*, e0178821.

Dobin, A., and Gingeras, T.R. (2015). Mapping RNA-seq reads with STAR. Curr. Protoc. Bioinformatics *51*, 1–19.

Dobin, A., Davis, C.A., Schlesinger, F., Drenkow, J., Zaleski, C., Jha, S., Batut, P., Chaisson, M., and Gingeras, T.R. (2013). STAR: ultrafast universal RNA-seq aligner. Bioinformatics *29*, 15–21.

Durinck, S., Moreau, Y., Kasprzyk, A., Davis, S., De Moor, B., Brazma, A., and Huber, W. (2005). BioMart and Bioconductor: a powerful link between biological databases and microarray data analysis. Bioinformatics *21*, 3439–3440.

Emanuelsson, O., Brunak, S., von Heijne, G., and Nielsen, H. (2007). Locating proteins in the cell using TargetP, SignalP and related tools. Nat. Protoc. *2*, 953–971.

Ewels, P., Magnusson, M., Lundin, S., and Käller, M. (2016). MultiQC: summarize analysis results for multiple tools and samples in a single report. Bioinformatics *32*, 3047–3048.

Fasken, M.B., and Corbett, A.H. (2009). Mechanisms of nuclear mRNA quality control. RNA Biol. *6*, 237–241.

Fazal, F.M., Han, S., Parker, K.R., Kaewsapsak, P., Xu, J., Boettiger, A., Chang, H.Y., and Ting, A.Y. (2019). APEX-seq: RNA subcellular localization by proximity labeling. Protocol Exchange. Published online May 15, 2019. https://doi.org/10.21203/rs.2.1857/v1.

Femino, A.M., Fay, F.S., Fogarty, K., and Singer, R.H. (1998). Visualization of single RNA transcripts in situ. Science *280*, 585–590.

Flynn, R.A., Zhang, Q.C., Spitale, R.C., Lee, B., Mumbach, M.R., and Chang, H.Y. (2016). Transcriptome-wide interrogation of RNA secondary structure in living cells with icSHAPE. Nat. Protoc. *11*, 273–290.

Fox, C.H., Johnson, F.B., Whiting, J., and Roller, P.P. (1985). Formaldehyde fixation. J. Histochem. Cytochem. *33*, 845–853.

Friedman, J.R., Lackner, L.L., West, M., DiBenedetto, J.R., Nunnari, J., and Voeltz, G.K. (2011). ER tubules mark sites of mitochondrial division. Science *334*, 358–362.

Gagnon, K.T., Li, L., Janowski, B.A., and Corey, D.R. (2014). Analysis of nuclear RNA interference in human cells by subcellular fractionation and Argonaute loading. Nat. Protoc. *9*, 2045–2060.

Gentleman, R.C., Carey, V.J., Bates, D.M., Bolstad, B., Dettling, M., Dudoit, S., Ellis, B., Gautier, L., Ge, Y., Gentry, J., et al. (2004). Bioconductor: open software development for computational biology and bioinformatics. Genome Biol. *5*, R80.

Giacomello, M., and Pellegrini, L. (2016). The coming of age of the mitochondria-ER contact: a matter of thickness. Cell Death Differ. *23*, 1417–1427.

Gold, V.A., Chroscicki, P., Bragoszewski, P., and Chacinska, A. (2017). Visualization of cytosolic ribosomes on the surface of mitochondria by electron cryotomography. EMBO Rep. *18*, 1786–1800.

Grünwald, D., and Singer, R.H. (2010). In vivo imaging of labelled endogenous β-actin mRNA during nucleocytoplasmic transport. Nature *467*, 604–607.

Gu, Z., Gu, L., Eils, R., Schlesner, M., and Brors, B. (2014). circlize Implements and enhances circular visualization in R. Bioinformatics *30*, 2811–2812.

Guelen, L., Pagie, L., Brasset, E., Meuleman, W., Faza, M.B., Talhout, W., Eussen, B.H., de Klein, A., Wessels, L., de Laat, W., and van Steensel, B. (2008). Domain organization of human chromosomes revealed by mapping of nuclear lamina interactions. Nature *453*, 948–951.

Han, S., Udeshi, N.D., Deerinck, T.J., Svinkina, T., Ellisman, M.H., Carr, S.A., and Ting, A.Y. (2017). Proximity biotinylation as a method for mapping proteins associated with mtDNA in living cells. Cell Chem. Biol. *24*, 404–414.

Han, S., Li, J., and Ting, A.Y. (2018). Proximity labeling: spatially resolved proteomic mapping for neurobiology. Curr. Opin. Neurobiol. *50*, 17–23.

Hansen, M.M.K., Desai, R.V., Simpson, M.L., and Weinberger, L.S. (2018). Cytoplasmic Amplification of Transcriptional Noise Generates Substantial Cell-to-Cell Variability. Cell Systems *7*, 384–397.

Hensen, F., Moretton, A., van Esveld, S., Farge, G., and Spelbrink, J.N. (2018). The mitochondrial outer-membrane location of the EXD2 exonuclease contradicts its direct role in nuclear DNA repair. Sci. Rep. *8*, 5368.

Hung, V., Zou, P., Rhee, H.-W., Udeshi, N.D., Cracan, V., Svinkina, T., Carr, S.A., Mootha, V.K., and Ting, A.Y. (2014). Proteomic mapping of the human mitochondrial intermembrane space in live cells via ratiometric APEX tagging. Mol. Cell *55*, 332–341.

Hung, V., Udeshi, N.D., Lam, S.S., Loh, K.H., Cox, K.J., Pedram, K., Carr, S.A., and Ting, A.Y. (2016). Spatially resolved proteomic mapping in living cells with the engineered peroxidase APEX2. Nat. Protoc. *11*, 456–475.

Hung, V., Lam, S.S., Udeshi, N.D., Svinkina, T., Guzman, G., Mootha, V.K., Carr, S.A., and Ting, A.Y. (2017). Proteomic mapping of cytosol-facing outer mitochondrial and ER membranes in living human cells by proximity biotinylation. eLife *6*. Published online April 25, 2017. https://doi.org/10.7554/eLife.24463.

Hwang, J., and Espenshade, P.J. (2016). Proximity-dependent biotin labelling in yeast using the engineered ascorbate peroxidase APEX2. Biochem. J. *473*, 2463–2469.

Ichiyanagi, K. (2013). Epigenetic regulation of transcription and possible functions of mammalian short interspersed elements, SINEs. Genes Genet. Syst. *88*, 19–29.

Ingolia, N.T., Ghaemmaghami, S., Newman, J.R., and Weissman, J.S. (2009). Genome-wide analysis in vivo of translation with nucleotide resolution using ribosome profiling. Science *324*, 218–223.

Jan, C.H., Williams, C.C., and Weissman, J.S. (2014). Principles of ER cotranslational translocation revealed by proximity-specific ribosome profiling. Science *346*, 1257521–1257521.

Kaewsapsak, P., Shechner, D.M., Mallard, W., Rinn, J.L., and Ting, A.Y. (2017). Live-cell mapping of organelle-associated RNAs via proximity biotinylation combined with protein-RNA crosslinking. eLife *6*. Published online December 14, 2017. https://doi.org/10.7554/eLife.29224.

Käll, L., Krogh, A., and Sonnhammer, E.L. (2004). A combined transmembrane topology and signal peptide prediction method. J. Mol. Biol. *338*, 1027–1036.

Karolchik, D., Hinrichs, A.S., Furey, T.S., Roskin, K.M., Sugnet, C.W., Haussler, D., and Kent, W.J. (2004). The UCSC Table Browser data retrieval tool. Nucleic Acids Res. *32*, D493–D496.

Kellems, R.E., Allison, V.F., and Butow, R.A. (1974). Cytoplasmic type 80 S ribosomes associated with yeast mitochondria. II. Evidence for the association of cytoplasmic ribosomes with the outer mitochondrial membrane in situ. J. Biol. Chem. *249*, 3297–3303.

Kellems, R.E., Allison, V.F., and Butow, R.A. (1975). Cytoplasmic type 80S ribosomes associated with yeast mitochondria. IV. Attachment of ribosomes to the outer membrane of isolated mitochondria. J. Cell Biol. *65*, 1–14.

Kent, W.J., Sugnet, C.W., Furey, T.S., Roskin, K.M., Pringle, T.H., Zahler, A.M., and Haussler, D. (2002). The human genome browser at UCSC. Genome Res. *12*, 996–1006.

Kent, W.J., Zweig, A.S., Barber, G., Hinrichs, A.S., and Karolchik, D. (2010). BigWig and BigBed: enabling browsing of large distributed datasets. Bioinformatics *26*, 2204–2207.

Kim, S.J., Fernandez-Martinez, J., Nudelman, I., Shi, Y., Zhang, W., Raveh, B., Herricks, T., Slaughter, B.D., Hogan, J.A., Upla, P., et al. (2018). Integrative structure and functional anatomy of a nuclear pore complex. Nature *555*, 475–482.

Krogh, A., Larsson, B., von Heijne, G., and Sonnhammer, E.L. (2001). Predicting transmembrane protein topology with a hidden Markov model: application to complete genomes. J. Mol. Biol. *305*, 567–580.

Lam, S.S., Martell, J.D., Kamer, K.J., Deerinck, T.J., Ellisman, M.H., Mootha, V.K., and Ting, A.Y. (2015). Directed evolution of APEX2 for electron microscopy and proximity labeling. Nat. Methods *12*, 51–54.

Lee, B., Flynn, R.A., Kadina, A., Guo, J.K., Kool, E.T., and Chang, H.Y. (2017). Comparison of SHAPE reagents for mapping RNA structures inside living cells. RNA *23*, 169–174.

Lex, A., Gehlenborg, N., Strobelt, H., Vuillemot, R., and Pfister, H. (2014). UpSet: visualization of intersecting sets. IEEE Trans. Vis. Comput. Graph. *20*, 1983–1992.

Li, H., Handsaker, B., Wysoker, A., Fennell, T., Ruan, J., Homer, N., Marth, G., Abecasis, G., and Durbin, R.; 1000 Genome Project Data Processing Subgroup (2009). The sequence alignment/map format and SAMtools. Bioinformatics *25*, 2078–2079.

Linden, A. (2006). Measuring diagnostic and predictive accuracy in disease management: an introduction to receiver operating characteristic (ROC) analysis. J. Eval. Clin. Pract. *12*, 132–139.

Loh, K.H., Stawski, P.S., Draycott, A.S., Udeshi, N.D., Lehrman, E.K., Wilton, D.K., Svinkina, T., Deerinck, T.J., Ellisman, M.H., Stevens, B., et al. (2016). Proteomic analysis of unbounded cellular compartments: synaptic clefts. Cell *166*, 1295–1307.

Love, M.I., Huber, W., and Anders, S. (2014). Moderated estimation of fold change and dispersion for RNA-seq data with DESeq2. Genome Biol. *15*, 550.

Lubelsky, Y., and Ulitsky, I. (2018). Sequences enriched in Alu repeats drive nuclear localization of long RNAs in human cells. Nature *555*, 107–111.

Ma, J., Liu, Z., Michelotti, N., Pitchiaya, S., Veerapaneni, R., Androsavich, J.R., Walter, N.G., and Yang, W. (2013). High-resolution three-dimensional mapping of mRNA export through the nuclear pore. Nat. Commun. *4*, 2414.

Maglott, D., Ostell, J., Pruitt, K.D., and Tatusova, T. (2011). Entrez Gene: gene-centered information at NCBI. Nucleic Acids Res. *39*, D52–D57.

Mayr, C. (2017). Regulation by 3′-Untranslated Regions. Annu. Rev. Genet. *51*, 171–194.

Mercer, T.R., Neph, S., Dinger, M.E., Crawford, J., Smith, M.A., Shearwood, A.M., Haugen, E., Bracken, C.P., Rackham, O., Stamatoyannopoulos, J.A., et al. (2011). The human mitochondrial transcriptome. Cell *146*, 645–658.

Meyer, K.D., Saletore, Y., Zumbo, P., Elemento, O., Mason, C.E., and Jaffrey, S.R. (2012). Comprehensive analysis of mRNA methylation reveals enrichment in 3′ UTRs and near stop codons. Cell *149*, 1635–1646.

Mi, H., Muruganujan, A., Casagrande, J.T., and Thomas, P.D. (2013). Large-scale gene function analysis with the PANTHER classification system. Nat. Protoc. *8*, 1551–1566.

Moffitt, J.R., and Zhuang, X. (2016). RNA Imaging with Multiplexed Error-Robust Fluorescence In Situ Hybridization (MERFISH). Methods Enzymol. *572*, 1–49.

Mortensen, A., and Skibsted, L.H. (1997). Importance of carotenoid structure in radical-scavenging reactions. J. Agric. Food Chem. *45*, 2970–2977.

Mou, Z., Tapper, A.R., and Gardner, P.D. (2009). The armadillo repeat-containing protein, ARMCX3, physically and functionally interacts with the developmental regulatory factor Sox10. J. Biol. Chem. *284*, 13629–13640.

Németh, A., Conesa, A., Santoyo-Lopez, J., Medina, I., Montaner, D., Péterfia, B., Solovei, I., Cremer, T., Dopazo, J., and Längst, G. (2010). Initial genomics of the human nucleolus. PLoS Genet. *6*, e1000889.

Padeken, J., Zeller, P., and Gasser, S.M. (2015). Repeat DNA in genome organization and stability. Curr. Opin. Genet. Dev. *31*, 12–19.

Pandey, R.R., Homolka, D., Chen, K.M., Sachidanandam, R., Fauvarque, M.O., and Pillai, R.S. (2017). Recruitment of Armitage and Yb to a transcript triggers its phased processing into primary piRNAs in Drosophila ovaries. PLoS Genet. *13*, e1006956.

Patel, A., Lee, H.O., Jawerth, L., Maharana, S., Jahnel, M., Hein, M.Y., Stoynov, S., Mahamid, J., Saha, S., Franzmann, T.M., et al. (2015). A liquid-to-solid phase transition of the ALS Protein FUS accelerated by disease mutation. Cell *162*, 1066–1077.

Pedregosa, F., Varoquaux, G., Gramfort, A., Michel, V., Thirion, B., Grisel, O., Blondel, M., Prettenhofer, P., et al. (2011). Scikit-learn: Machine Learning in Python. J. Mach. Learn. Res. *12*, 2825–2830.

Penny, G.D., Kay, G.F., Sheardown, S.A., Rastan, S., and Brockdorff, N. (1996). Requirement for Xist in X chromosome inactivation. Nature *379*, 131–137.

Petersen, T.N., Brunak, S., von Heijne, G., and Nielsen, H. (2011). SignalP 4.0: discriminating signal peptides from transmembrane regions. Nat. Methods *8*, 785–786.

Pimentel, H., Bray, N.L., Puente, S., Melsted, P., and Pachter, L. (2017). Differential analysis of RNA-seq incorporating quantification uncertainty. Nat. Methods *14*, 687–690.

Pruitt, K.D., Tatusova, T., and Maglott, D.R. (2007). NCBI reference sequences (RefSeq): a curated non-redundant sequence database of genomes, transcripts and proteins. Nucleic Acids Res. *35*, D61–D65.

Quinlan, A.R., and Hall, I.M. (2010). BEDTools: a flexible suite of utilities for comparing genomic features. Bioinformatics *26*, 841–842.

Reck-Peterson, S.L., Redwine, W.B., Vale, R.D., and Carter, A.P. (2018). The cytoplasmic dynein transport machinery and its many cargoes. Nat. Rev. Mol. Cell Biol. *19*, 382–398.

Reid, D.W., and Nicchitta, C.V. (2012). Primary role for endoplasmic reticulum-bound ribosomes in cellular translation identified by ribosome profiling. J. Biol. Chem. *287*, 5518–5527.

Reid, D.W., and Nicchitta, C.V. (2015). Diversity and selectivity in mRNA translation on the endoplasmic reticulum. Nat. Rev. Mol. Cell Biol. *16*, 221–231.

Reinke, A.W., Mak, R., Troemel, E.R., and Bennett, E.J. (2017). In vivo mapping of tissue- and subcellular-specific proteomes in *Caenorhabditis elegans*. Sci. Adv. *3*, e1602426.

Rhee, H.W., Zou, P., Udeshi, N.D., Martell, J.D., Mootha, V.K., Carr, S.A., and Ting, A.Y. (2013). Proteomic mapping of mitochondria in living cells via spatially restricted enzymatic tagging. Science *339*, 1328–1331.

Roundtree, I.A., Luo, G.Z., Zhang, Z., Wang, X., Zhou, T., Cui, Y., Sha, J., Huang, X., Guerrero, L., Xie, P., et al. (2017). YTHDC1 mediates nuclear export of N^6-methyladenosine methylated mRNAs. eLife *6*. Published online October 6, 2017. https://doi.org/10.7554/eLife.31311.

Sadowski, P.G., Groen, A.J., Dupree, P., and Lilley, K.S. (2008). Sub-cellular localization of membrane proteins. Proteomics *8*, 3991–4011.

Schneider, C.A., Rasband, W.S., and Eliceiri, K.W. (2012). NIH Image to ImageJ: 25 years of image analysis. Nat. Methods *9*, 671–675.

Schnell, U., Dijk, F., Sjollema, K.A., and Giepmans, B.N.G. (2012). Immunolabeling artifacts and the need for live-cell imaging. Nat. Methods *9*, 152–158.

Shah, S., Lubeck, E., Zhou, W., and Cai, L. (2016). In situ transcription profiling of single cells reveals spatial organization of cells in the mouse hippocampus. Neuron *92*, 342–357.

Shen, S., Park, J.W., Lu, Z.X., Lin, L., Henry, M.D., Wu, Y.N., Zhou, Q., and Xing, Y. (2014). rMATS: robust and flexible detection of differential alternative splicing from replicate RNA-Seq data. Proc. Natl. Acad. Sci. USA *111*, E5593–E5601.

Shen, J., Zhang, J.H., Xiao, H., Wu, J.M., He, K.M., Lv, Z.Z., Li, Z.J., Xu, M., and Zhang, Y.Y. (2018). Mitochondria are transported along microtubules in membrane nanotubes to rescue distressed cardiomyocytes from apoptosis. Cell Death Dis. *9*, 81.

Shukla, C.J., McCorkindale, A.L., Gerhardinger, C., Korthauer, K.D., Cabili, M.N., Shechner, D.M., Irizarry, R.A., Maass, P.G., and Rinn, J.L. (2018). High-throughput identification of RNA nuclear enrichment sequences. EMBO J. *37*. Published online March 15, 2018. https://doi.org/10.15252/embj.201798452.

Spitale, R.C., Flynn, R.A., Zhang, Q.C., Crisalli, P., Lee, B., Jung, J.-W., Kuchelmeister, H.Y., Batista, P.J., Torre, E.A., Kool, E.T., and Chang, H.Y. (2015). Structural imprints in vivo decode RNA regulatory mechanisms. Nature *519*, 486–490.

Subtelny, A.O., Eichhorn, S.W., Chen, G.R., Sive, H., and Bartel, D.P. (2014). Poly(A)-tail profiling reveals an embryonic switch in translational control. Nature *508*, 66–71.

Sultan, M., Amstislavskiy, V., Risch, T., Schuette, M., Dökel, S., Ralser, M., Balzereit, D., Lehrach, H., and Yaspo, M.L. (2014). Influence of RNA extraction methods and library selection schemes on RNA-seq data. BMC Genomics *15*, 675.

Sun, L., Fazal, F.M., Li, P., Broughton, J.P., Lee, B., Tang, L., Huang, W., Kool, E.T., Chang, H.Y., and Zhang, Q.C. (2019). RNA structure maps across mammalian cellular compartments. Nat. Struct. Mol. Biol. *26*, 322–330.

Thomas, P.D., Campbell, M.J., Kejariwal, A., Mi, H., Karlak, B., Daverman, R., Diemer, K., Muruganujan, A., and Narechania, A. (2003). PANTHER: a library of protein families and subfamilies indexed by function. Genome Res. *13*, 2129–2141.

Thul, P.J., Åkesson, L., Wiking, M., Mahdessian, D., Geladaki, A., Ait Blal, H., Alm, T., Asplund, A., Björk, L., Breckels, L.M., et al. (2017). A subcellular map of the human proteome. Science *356*. Published online May 26, 2017. https://doi.org/10.1126/science.aal3321.

Tibshirani, R., Walther, G., and Hastie, T. (2001). Estimating the number of clusters in a data set via the gap statistic. J. R. Stat. Soc. B *63*, 411–423.

Valm, A.M., Cohen, S., Legant, W.R., Melunis, J., Hershberg, U., Wait, E., Cohen, A.R., Davidson, M.W., Betzig, E., and Lippincott-Schwartz, J. (2017). Applying systems-level spectral imaging and analysis to reveal the organelle interactome. Nature *546*, 162–167.

van der Maaten, L., and Hinton, G. (2008). Visualizing data using t-SNE. J. Mach. Learn. Res. *9*, 2579–2605.

van Koningsbruggen, S., Gierlinski, M., Schofield, P., Martin, D., Barton, G.J., Ariyurek, Y., den Dunnen, J.T., and Lamond, A.I. (2010). High-resolution whole-genome sequencing reveals that specific chromatin domains from most human chromosomes associate with nucleoli. Mol. Biol. Cell *21*, 3735–3748.

Van Nostrand, E.L., Pratt, G.A., Shishkin, A.A., Gelboin-Burkhart, C., Fang, M.Y., Sundararaman, B., Blue, S.M., Nguyen, T.B., Surka, C., Elkins, K., et al. (2016). Robust transcriptome-wide discovery of RNA-binding protein binding sites with enhanced CLIP (eCLIP). Nat. Methods *13*, 508–514.

van Steensel, B., and Belmont, A.S. (2017). Lamina-associated domains: links with chromosome architecture, heterochromatin, and gene repression. Cell *169*, 780–791.

Walther, T.C., Fornerod, M., Pickersgill, H., Goldberg, M., Allen, T.D., and Mattaj, I.W. (2001). The nucleoporin Nup153 is required for nuclear pore basket formation, nuclear pore complex anchoring and import of a subset of nuclear proteins. EMBO J. *20*, 5703–5714.

Weil, T.T., Parton, R.M., and Davis, I. (2010). Making the message clear: visualizing mRNA localization. Trends Cell Biol. *20*, 380–390.

Wheeler, T.J., Clements, J., Eddy, S.R., Hubley, R., Jones, T.A., Jurka, J., Smit, A.F., and Finn, R.D. (2013). Dfam: a database of repetitive DNA based on profile hidden Markov models. Nucleic Acids Res. *41*, D70–D82.

Wickham, H. (2009). ggplot2: Elegant Graphics for Data Analysis (Springer).

Wickramasinghe, V.O., and Laskey, R.A. (2015). Control of mammalian gene expression by selective mRNA export. Nat. Rev. Mol. Cell Biol. *16*, 431–442.

Williams, C.C., Jan, C.H., and Weissman, J.S. (2014). Targeting and plasticity of mitochondrial proteins revealed by proximity-specific ribosome profiling. Science *346*, 748–751.

Wishart, J.F., and Rao, B.S.M. (2010). Recent Trends in Radiation Chemistry (World Scientific).

Zuker, M. (2003). Mfold web server for nucleic acid folding and hybridization prediction. Nucleic Acids Res. *31*, 3406–3415.

STAR★METHODS

KEY RESOURCES TABLE

REAGENT or RESOURCE	SOURCE	IDENTIFIER
Antibodies		
Anti V5	Life Technologies	Cat# R96025; RRID: AB_2556564
Anti FLAG	Agilent	Cat# 200472; RRID: AB_10596649
Anti TOM20	Santa Cruz Biotechnology	Cat# SC-11415; RRID: AB_2207533
AlexaFlour488	Life Technologies	Cat# A11029; RRID: AB_2534088
AlexaFluor568	Life Technologies	Cat# A11036; RRID: AB_10563566
AlexaFluor647	Invitrogen	Cat# A20006
Neutravidin biotin-binding protein	Invitrogen	Cat# A2666
Calnexin	Thermofischer	Cat# PA534754; RRID: AB_2552106
Streptavidin IRDye 800CW (green)	LI-COR	Cat# 926-32230
Chemicals, Peptides, and Recombinant Proteins		
Sodium ascorbate	Sigma Aldrich	Cat# A7631-25G
Trolox	Sigma Aldrich	Cat# 238813-1G
Biotin tyramide	Iris Biotech Gmbh	Cat# LS3500
Agencourt AMPure XP	Beckman Coulter	Cat# A63881
Pierce streptavidin magnetic beads	Thermo Fischer Scientific	Cat# 88816
Lipofectamine 2000	Thermo Fischer Scientific	Cat# 11668019
TURBO DNase	Thermo Fischer Scientific	Cat# AM2238
Fibronectin	Millipore	Cat# FC010
Superscript III first-strand synthesis system	Thermo Fischer Scientific	Cat# 18080051
Proteinase K solution (20 mg/ml)	Life Technologies	Cat# AM2548
RiboLock RNase inhibitor	Thermo Scientific	Cat# EO0384
Buffer RWT	QIAGEN	Cat# 1067933
DTT (dithiothreitol)	Thermo Fisher Scientific	Cat# R0861
N-Lauroylsarcosine sodium salt solution	Sigma-Aldrich	Cat# L7414-10ML
Hydrogen peroxide solution, 30% (w/w)	Sigma-Aldrich	Cat# H1009-100ML
Nocodazole	Sigma-Aldrich	Cat# M1404-10MG
Cycloheximide	Sigma-Aldrich	Cat# 01810-1G
Puromycin	VWR	Cat# 80054-138
CCCP	Sigma-Aldrich	Cat# C2759-100MG
Low Range ssRNA Ladder	NEB	Cat# N0364S
P32 ATP 6000units 250uCi	PerkinElmer	NEG502Z250UC
Amersham Protran 0.45 nitrocellulose	GE Healthcare	Cat# 10600033
Critical Commercial Assays		
Truseq RNA sample preparation kit v2	Illumina	RS-122-2001
RNeasy Plus mini kit	QIAGEN	Cat# 74136
RNA Clean and concentrator-5	Zymo Research	Cat# R1016
MEGAscript T7 transcription kit	Ambion	Cat# AM1334
MEGAclear transcription clean-up kit	Thermo Fisher Scientific	Cat# AM1908
Miseq reagents kit v3	Illumina	Cat# MS-102-3001
Deposited Data		
Raw and analyzed data	This paper	GEO: GSE116008
HEK293 m6A sites (MeRIP-seq)	Meyer et al., 2012	PMID: 22608085

(*Continued on next page*)

Continued

REAGENT or RESOURCE	SOURCE	IDENTIFIER
HEK293 ER proximity-specific ribosome profiling RNA-seq	Jan et al., 2014	PMID: 25378630
HEK293 ER fractionation RNA-seq	Reid and Nicchitta, 2015	PMID: 22199352
HEK293 RNA-seq	Sultan et al., 2014	ERA: PRJEB4197
HEK293 APEX-RIP data	Kaewsapsak et al., 2017	PMID: 29239719
HEK293 polyA-tail length	Subtelny et al., 2014	GEO: GSE52809
Protein localization data	Thul et al., 2017	PMID: 28495876
OMM APEX proteomics data	Hung et al., 2017	PMID: 28441135
Dfam database	Wheeler et al., 2013	https://dfam.org/
Human LADs	Guelen et al., 2008	PMID: 18463634
Human NADs	Németh et al., 2010	PMID: 20361057
Human NADs	Dillinger et al., 2017	PMID: 28575119
GO enrichment analysis	Thomas et al., 2003	http://www.pantherdb.org/
Human mitochondrial genes (Mitocarta 2.0)	Calvo et al., 2016	PMID: 26450961
Signal peptide annotations (SignalP 4.0)	Petersen et al., 2011	PMID: 21959131
Signal peptide annotations (Phobius)	Käll et al., 2004	PMID: 15111065
Transmembrane protein annotations (TMHMM)	Krogh et al., 2001	http://www.cbs.dtu.dk/services/TMHMM/
Experimental Models: Cell Lines		
HEK293T	ATCC	Cat# CRL-3216
Oligonucleotides		
Primers used	This study	Table S1
5S RNA gDNA block	This study	Table S1
seqFISH oligos	Chen et al., 2015b	https://github.com/ZhuangLab/MERFISH_analysis
Recombinant DNA		
ERM-APEX2	Addgene	Plasmid #79055
APEX2-OMM	Addgene	Plasmid #79056
APEX2-NES	Addgene	Plasmid #92158
Mito-APEX2	Addgene	Plasmid #72480
APEX2-NLS	Kaewsapsak et al., 2017	NotI-V5-APEX2-EcoRI-3xNLS-NheI CMV promoter NLS: DPKKKRKV
HRP-KDEL	Kaewsapsak et al., 2017	NotI-IgK-HRP-V5-KDEL-IRES -puromycin-XbaI CMV promoter IgK is N-terminal signaling sequence that brings protein to ER (METDTLLLWVLLLWVPGSTGD). KDEL is ER-retaining sequence
APEX2-LMNA	This study	BstBI-V5-APEX2-LMNA-NheI CMV promoter LMNA: prelamin-A/C
APEX2-SENP2	This study	BstBI-V5-APEX2-SENP2-NheI CMV promoter SENP2: Sentrin-specific Protease 2
APEX2-NIK3x	This study	BstBI-EGFP-APEX2-3xNIK-NheI CMV promoter NIK: Nucleolar targeting sequence from NIK
Software and Algorithms		
STAR	Dobin et al., 2013	RRID: SCR_015899
t-SNE	van der Maaten and Hinton, 2008	RRID: SCR_016900
HTSeq	Anders et al., 2014	RRID: SCR_005514
Bioconductor	Gentleman et al., 2004	RRID: SCR_006442
DESeq2	Love et al., 2014	RRID: SCR_015687
Ggplot2	Wickham, 2009	RRID: SCR_014601

(*Continued on next page*)

Continued

REAGENT or RESOURCE	SOURCE	IDENTIFIER
Barcode trimming	Flynn et al., 2016	PMID: 26766114
ImageJ	Schneider et al., 2012	https://imagej.nih.gov/ij/
SAMtools	Li et al., 2009	PMID: 19505943
Bedtools	Quinlan and Hall, 2010	RRID: SCR_006646
Kallisto	Bray et al., 2016	RRID: SCR_016582
scikit-learn package	Pedregosa et al., 2011	RRID: SCR_002577
PolyA_SVM package	Cheng et al., 2006	PMID: 16870936
MultiQC package	Ewels et al., 2016	RRID: SCR_014982
rMATS	Shen et al., 2014	RRID: SCR_013049
Sleuth	Pimentel et al., 2017	RRID: SCR_016883
DEXSeq	Anders et al., 2012	RRID: SCR_012823
circlize	Gu et al., 2014	RRID: SCR_002141
Other		
Detailed APEX-seq library protocol	This paper; Fazal et al., 2019	Protocol Exchange https://doi.org/10.21203/rs.2.1857/v1

LEAD CONTACT AND MATERIALS AVAILABILITY

Further information and requests for resources and reagents should be directed to and will be fulfilled by the Lead Contact, Alice Y. Ting (ayting@stanford.edu).

EXPERIMENTAL MODEL AND SUBJECT DETAILS

Mammalian cell culture

HEK293T cells from the ATCC (passages <25) were cultured in a 1:1 DMEM/MEM mixture (Cellgro) supplemented with 10% fetal bovine serum, 100 units/mL penicillin, and 100 mg/mL streptomycin at 37°C under 5% CO_2 (Hung et al., 2016). Mycoplasma testing was not performed before experiments. For fluorescence microscopy imaging experiments, cells were grown on 7 × 7-mm glass coverslips in 48-well plates. For qPCR and RNA-seq experiments, cells were grown on 10-cm glass-bottomed Petri dishes (Corning). To improve the adherence of HEK293T cells, we pretreated glass slides with 50 μg/mL fibronectin (Millipore) for 20 min at 37°C before cell plating and washing three times with Dulbecco's PBS (DPBS) (pH 7.4).

Generation of HEK293T cells stably expressing different APEX2 constructs

APEX2 fusion constructs in Figure S2A were cloned into pLX304 vector via Gibson assembly. For preparation of lentiviruses, HEK293T cells in 6-well plates were transfected at ~60%–70% confluency with the lentiviral vector pLX304 containing the gene of interest (1,000 ng), the lentiviral packaging plasmids dR8.91 (900 ng) and pVSV-G (100 ng), and 8 μL of Lipofectamine 2000 for 4 h (Hung et al., 2016). About 48 h after transfection the cell medium containing lentivirus was harvested and filtered through a 0.45-mm filter. HEK293T cells were then infected at ~50% confluency, followed by selection with 8 mg/mL blasticidin in growth medium for 7 days before further analysis.

METHOD DETAILS

APEX labeling in living cells

18-24 h after plating HEK293T cells stably expressing the corresponding APEX2 fusion construct, APEX labeling was initiated by changing the medium to fresh medium containing 500 μM biotin-phenol (Iris Biotech GMBH). This was incubated at 37°C under 5% CO_2 for 30 min. H_2O_2 (Sigma Aldrich) was then added to each well to a final concentration of 1 mM, and the plate gently agitated for 1 min (Hung et al., 2016). The reaction was quenched by replacing the medium with an equal volume of 5 mM Trolox, 10 mM sodium ascorbate and 10 mM sodium azide in Dulbecco's phosphate-buffered saline (DPBS). Cells were washed with DPBS containing 5 mM Trolox and 10 mM sodium ascorbate three times before proceeding to imaging, RT-qPCR or RNA-seq experiments. The unlabeled controls were processed identically, except that the H_2O_2 addition step was omitted.

Immunofluorescence staining and fluorescence microscopy

Cells were fixed with 4% paraformaldehyde in PBS at room temperature for 15 min. Cells were then washed with PBS three times and permeabilized with cold methanol at –20°C for 5-10 min. Cells were washed again three times with PBS and blocked for 1 h with 3% BSA in PBS ("blocking buffer") at room temperature. Cells were then incubated with primary antibodies (Mouse anti-V5 antibody, Life

Technologies, 1:1000 dilution; Mouse anti-FLAG antibody, Agilent, 1:1000 dilution; Rabbit anti-TOM20 antibody, Santa Cruz Biotechnology, 1:800 dilution; Rabbit anti-Calnexin antibody, Life Technologies, 1:1000 dilution) in blocking buffer for 1 h at room temperature. After washing three times with PBS, cells were incubated with secondary antibodies (AlexaFluor488, Life Technologies 1:1000 dilution; AlexaFluor568, Life Technologies 1:1000 dilution; neutravidin-AlexaFluor647, Life Technologies, 1:1000 dilution) in blocking buffer for 30 min. Cells were then washed three times with PBS and imaged. Fluorescence confocal microscopy was performed with a Zeiss AxioObserver microscope with 60X oil immersion objectives, outfitted with a Yokogawa spinning disk confocal head, Cascade II:512 camera, a Quad-band notch dichroic mirror (405/488/568/647), and 405 (diode), 491 (DPSS), 561 (DPSS) and 640 nm (diode) lasers (all 50 mW). CFP (405 laser excitation, 445/40 emission), Venus/Alexa Fluor488 (491 laser excitation, 528/38 emission), AlexaFluor568 (561 laser excitation, 617/73 emission), and AlexaFluor647 (640 laser excitation, 700/75 emission) and differential interference contrast (DIC) images were acquired through a 60x oil-immersion lens. Acquisition times ranged from 100 to 2,000 ms (ms).

RNA extraction for RT-qPCR or RNA-seq

To labeled and unlabeled (controls) HEK293T cells in 10-cm plates, we added ~1 mL DPBS containing 5 mM Trolox and 10 mM sodium ascorbate, as well as ~4 uL Ribolock RNase inhibitor (Thermo Fischer). The cells were then scrapped off 10-cm plates using cell lifters (Corning), transferred to 2-mL Eppendorf tubes, and spun at ~300G for 4 min to pellet cells. The supernatant was removed, and the RNA was extracted from cells using the RNeasy plus mini kit (QIAGEN) following the manufacture protocol, including adding β-mercaptoethanol to the lysis buffer. The cells were sent through the genomic DNA (gDNA) eliminator column supplied with the kit. A modification to the protocol was replacing the RW1 buffer with RWT buffer (QIAGEN) for washing. The extracted RNA was eluted into RNase-free water, and RNA integrity was checked using the Agilent bioanalyzer 2100 using the RNA pico assay. Only RNA with a RIN (RNA integrity number) > 8.5 was used for subsequent experiments. RNAs shorter than 100 nt were not efficiently recovered. RNA concentrations were determined using the Nanodrop (Thermo Fischer).

APEX labeling streptavidin dot blot experiment

RNA from labeled NES-APEX2 (cytosol) HEK293T cells was treated with Turbo DNase (Thermo Fischer) at 37°C for 30 min, followed by purification using the RNA clean and concentrator −5 kit (Zymo Research). ~500 ng of purified RNA was blotted on the Amersham Protran 0.45 nitrocellulose (NC) membrane, and the membrane allowed to sit for at least 15 min to allow liquid to dry. The RNA was crosslinked to the membrane using 2500 μJ energy (254 nm wavelength, UV Stratalinker 2400) (Spitale et al., 2015). The membrane was then wet with ~5 mL PBST (PBS-TWEEN 20), followed by incubation with 15 mL PBST containing 1 μL LI-COR Streptavidin IRDye 800CW (green). The membrane was washed thrice with PBS and imaged on the LI-COR Odyssey CLX. For the RNase digestion, we treated the RNA with RNase cocktail enzyme mix (Ambion) for 30 min at room temperature (RT), followed by purification using the RNA clean and concentrator kit.

All RNA experiments were carried out using standard protocols to minimize and eliminate RNase contamination. These included using a dedicated work area for RNA, using filtered pipette tips, wiping all surfaces with RNase Zap (Invitrogen), using certified RNase-free buffers and reagents, and testing buffers for RNase contamination using RNase Alert (Ambion). When appropriate, ~1-2 μL of Ribolock RNase inhibitor (Thermo Fischer) was added per 100-200 μL of buffer/solution.

Horseradish peroxidase (HRP) *in vitro* labeling

For *in vitro* labeling, 100 μg of yeast tRNA extract (Thermo Fischer) were incubated with 500 μM BP, 1 mM H_2O_2, and 2.25 μM HRP (Thermo Fischer) in PBS for 1 min. The reaction was quenched by adding a PBS solution with final concentration of 10 mM sodium azide, 10 mM sodium ascorbate, and 5 mM Trolox. The reaction was cleaned up by the RNA clean and concentrator −5 kit (Zymo Research). For RNA digestion, 15 μg of labeled RNA was incubated with 2.5 μg RNase A (Thermo Fischer) in total volume 25 μL in water. After 1 h at room temperature, the reaction was cleaned up by RNA clean and concentrator kit. For proteinase K digestion, 15 μg of labeled RNA was incubated with 50 μg of Protease K (Ambion) in a total volume 25 μL in PBS. After 1 h at 37°C, the reaction was cleaned up by RNA clean and concentrator kit. 1 μg of RNA was spotted for each condition and then dot-blotted as described above.

Enrichment of biotinylated RNA

To enrich biotinylated RNAs we used Pierce streptavidin magnetic beads (Thermo Fischer), using 10 μl beads per 25 μg of RNA. In general, RNA from half a 10-cm plate (~30-50 μg) was sufficient for generating high-quality polyA+ RNA-seq libraries. The beads were washed 3 times in B&W buffer (5 mM Tris-HCl, pH = 7.5, 0.5 mM EDTA, 1 M NaCl, 0.1% TWEEN 20 [Sigma Aldrich]), followed by 2 times in Solution A (0.1 M NaOH and 0.05 M NaCl), and 1 time in Solution B (0.1 M NaCl). The beads were then suspended in ~100-150 μL 0.1 M NaCl and incubated with ~100-125 μl RNA (diluted in water) on a rotator for 2 h at 4°C. The beads were then placed on a magnet and the supernatant discarded. Beads were washed 3 times in B&W buffer and resuspended in 54 μl water. A 3X proteinase digestion buffer was made (1.1 mL buffer contained 330 μl 10X PBS pH = 7.4 (Ambion), 330 uL 20% N-Lauryl sarcosine sodium solution (Sigma Aldrich), 66 μL 0.5M EDTA, 16.5 μL 1M dithiothreitol (DTT, Thermo Fischer) and 357.5 μL water). 33 uL of this 3X proteinase buffer was added to the beads along with 10 μl Proteinase K (20 mg/mL, Ambion) and 3 μL Ribolock RNase inhibitor. The beads were then incubated at 42°C for 1 h, followed by 55°C for 1 h on a shaker. The RNA was then purified using the RNA clean and concentrator −5 kit (Zymo Research). The RNA was typically not bioanalyzed but used as is for downstream applications.

APEX-seq library preparation

RNA-seq libraries were prepared from enriched RNA (corresponding to ~30-50 μg of pre-enriched RNA) using the Illumina TruSeq stranded mRNA preparation kit, which included polyA+ selection. The prepared libraries were stranded and were quality-controlled by sequencing on the Illumina MiSeq. Good libraries (> 80% unique reads) were sequenced on the Illumina Hiseq 4000 at ~40 million paired (2 × 75) reads per library. The polyA+ libraries (41 ± 2 million paired reads, mean ± SEM) had high mapping in both targets (90 ± 1% uniquely mapped reads) and controls (86 ± 1% uniquely mapped reads) (Figure S2C). The correlation between biological replicates was high (between 0.96 and 1). For the MITO APEX-seq we also generated total RNA samples (by omitting the polyA+ selection step in the TruSeq protocol), as well as a polyA+ selected technical replicate for 1 of the labeled samples.

Alternative enrichment strategies tested

We tested alternative strategies to enrich the biotinylated RNAs, and the best one (maximizing enrichment while minimizing material loss) is described above. In general, we found using harsh reagents such as formamide or urea increased yield variability across replicates while reducing yield. We varied temperature (RT versus 4°C), buffers used to wash beads, and amount and type of beads used (Pierce streptavidin beads versus Dyna MyOne Streptavidin C1 beads [Thermo Fischer]). Specifically, the protocols tested were as follows:

(1) Published APEX-RIP protocol/urea wash/high salt wash (Kaewsapsak et al., 2017) – 2 h 4°C incubation – 10 uL Pierce beads
(2) APEX-RIP protocol (excluding urea) – 2 h 4°C incubation – 10 uL Pierce beads
(3) APEX-RIP protocol – 10-15 min RT incubation – 10 uL Pierce beads
(4) APEX-RIP protocol – 2 h 4°C incubation – 10 uL Pierce beads – +2 additional washes of 50% formamide for 15 min at 37°C
(5) High salt wash (described above, B&W buffer) – 15 min at RT – 150 uL Dyna beads
(6) High salt wash – 15 min at RT – 10 uL Pierce beads
(7) APEX-RIP protocol – 2 h 4°C incubation – 50 uL Pierce beads
(8) APEX-RIP protocol – 2 h 4°C incubation – 10 uL Pierce beads – +2 washes 20% formamide for 15 min at 37°C)
(9) High salt wash – 2 h 4°C incubation – 10 uL Pierce beads (finalized protocol)
(10) High salt wash – with 2 h 4°C incubation – 10 uL Pierce beads – + 2 M urea wash
(11) No enrichment controls

Formamide was in 1X SSC buffer (Promega). For APEX-RIP protocol, we used RIPA buffer, 1 M KCl and 2M Urea buffers, following the APEX-RIP protocol (Kaewsapsak et al., 2017).

APEX RT-qPCR experiments (MITO)

To test for APEX RNA enrichment, we designed primers against positives (*MTND1* and *MTCO2*) and negatives (*GAPDH*, *SSR2*, *XIST*, *FAU*). The sequences of the primers (purchased from Elim Biopharmaceuticals) are listed in Table S1.

For the RT-qPCR experiments, the enriched MITO-APEX2 RNA was first reverse transcribed following the Superscript III reverse transcriptase (Thermo Fischer) protocol using random hexamers as primers (Kaewsapsak et al., 2017). The resulting cDNA was then testing using qPCR using the primers above in 2X SYBR Green PCR Master Mix (Thermo Fischer), with data generated on Lightcycler 480 (Roche). For each RNA we calculated the ratio of RNA recovered in the labeled target relative to unlabeled controls. We then calculated enrichment as recovery of positives relative to negatives, correcting for primer efficiency (> 85% for all primers).

APEX RT-qPCR experiments (ERM)

To confirm enrichment of known secretory RNAs by ERM APEX-seq, we designed primers against known secretory (SSR2, TMX1 and SFT2D2) and non-secretory genes (FAU, SUB1, MTCO2). The sequences of the primers (purchased from Sigma Aldrich) are listed in Table S1.

APEX-RIP RT-qPCR experiments with ERM-APEX2 stable cells were performed as described previously (Kaewsapsak et al., 2017). Briefly HEK293T cells stably expressing ERM-APEX2 were incubated with BP for 30 min prior to 1-min H_2O_2 labeling. 0.1% (v/v, in PBS) formaldehyde with 10 mM ascorbate and 5 mM Trolox was then added for 10 min to quench the reaction and crosslink the RNAs to proteins. The crosslinking reaction was terminated by the addition of 125 mM of glycine for 5 min. Following cell lysis in RIPA buffer, streptavidin beads were used to enrich the biotinylated material for 2 h at 4°C. The crosslinked RNAs and proteins were then reverse crosslinked before protein digestion with proteinase K. The subsequently purified RNA was analyzed by RT-qPCR.

RT-PCR of *in vitro* 5S RNA to map labeling positions

5S RNA was *in vitro* transcribed as follows. First, a gBlock Gene Fragments (Integrated DNA Technologies) was purchased with the human 5S RNA sequence adjacent to an overhang region (underlined):

ATATGCAAGCAACCCAAGTGGTCTACGGCCATACCACCCTGAACGCGCCCGATCTCGTCTGATCTCGGAAGCTAAGCAGGGT
CGGGCCTGGTTAGTACTTGGATGGGAGACCGCCTGGGAATACCGGGTGCTGTAGGCTTT

The DNA was amplified by PCR using Phusion High-fidelity DNA polymerase (NEB) and cleaned up using the QIAquick PCR purification kit (QIAGEN). The primers used for amplification are listed in Table S1. The DNA template was used to synthesize RNA using the MEGAscript Transcription T7 Kit (Thermo Fischer), and the transcribed RNA was purified using the MEGAclear kit (Ambion). The integrity and size of the transcribed RNA was checked by running the products on a 6% native agarose gel, stained with SYBR Gold (Thermo Fischer), and imaged using Molecular Imaging System (Biorad). All experiments were carried out using replicates. The labeled RNA was enriched using streptavidin-biotin pulldown as described above, and relative to unlabeled RNA the yield after enrichment and cleanup was 0.11 ± 0.02 (N = 2), as determined by the Nanodrop (Thermo Fischer).

We prepared labeled reverse primer following the USB Optikinase protocol (Affymetrix) using gamma-^{32P} ATP (Perkin Elmer). We added ^{32}P end-labeled reverse primer to ~100 ng RNA (labeled and controls), and the reaction mixture was heated at 95°C for 2 min followed by slow cool to 4°C at 10°C/mi, to facilitate annealing of primer (1 μL) to the RNA. The primer extension reaction was then initiated with reaction mix, as previously described (Lee et al., 2017). Briefly, the reaction mix (20 μL total; 4 μL 5X first strand buffer (FS), 1 μL 100mM DTT, 1 μL Ribolock inhibitor, 10 μL RNA, and 2 μL water) was added and the mixture preincubated at 52°C for 1 min before adding Superscript III (1 μL; 200 units, Invitrogen). Separately, similar reactions were carried out spiking in dATP with ddATP (dideoxyadenosine), and dCTP with ddCTP (dideoxycytidine), as described (Lee et al., 2017). Primer extension was carried out at 52°C for 30 min, after which the reaction was stopped by heating to 95°C for 5 min, followed by cooling to 4°C. The RNA was then hydrolyzed using NaOH (4M; 1 μL) and heating to 95°C for 5 min.

To the cDNA, Gel Loading Buffer II (10 μL; Invitrogen) was added, and the products run on a 35-cm long denaturing 8% polyacrylamide gel with 7M Urea (Thermo Fischer) (Lee et al., 2017). The resulting gel was dried (Labconco Gel Dryer) after placing it on Whatman paper (Sigma Aldrich) and exposed to a storage phosphor screen (Molecular Dynamics) for ~24 h, and then visualized by phosphorimaging (STORM, Molecular Dynamics). The lanes containing ddATP (corresponding transcribed RNA nucleotide U) and ddCTP (corresponding transcribed RNA nucleotide C) were used to determine the position of all RT stops. RNA secondary structures were predicted using mFOLD software (Zuker, 2003). The gel analysis was carried out using ImageJ (Schneider et al., 2012).

Liquid-chromatography (LC)-mass-spectrometry (MS) characterization of *in vitro* reaction products

2 mM dG (Sigma Aldrich) was incubated with 100 μM pentachlorophenol (PCP, Sigma Aldrich) or BP in PBS at 37°C for 1 h in the presence of 2.25 μM HRP or APEX2 and 100 μM H_2O_2. The reaction was diluted with water to final volume 100 μL and injected into an LC-MS with Zorbax Poroshell 120 SB-C18, 2.1 × 50 mm 2.7 u column with Poroshell 120 SB-C18 2.1 × 5 mm 2.7 u guard column. The gradient for LC is shown in the table below. Mass was determined by single quadruple mass spectrometry with positive and negative atmospheric pressure chemical ionization (APCI) and electrospray ionization (ESI) modes for M/Z = 20-2000.

Time (min)	Flow (mL/min)	% solvent A	% solvent B
0	0.3	98	2
2	0.3	98	2
6	0.3	5	95
8	0.3	5	95
8.5	0.3	98	2
9.5	0.3	5	95
10.5	0.3	5	95
11	0.3	98	2
15	0.3	98	2

Solvent A = 0.1% formic acid in water. Solvent B = 0.1% formic acid in acetonitrile.

Mapping and visualizing APEX-seq data

The RNA-seq libraries generated were mapped to the genome rather than to annotated transcriptome, so we could investigate intron retention. The RNA-seq reads were initially subject to barcode removal and primer trimming using a published script (Flynn et al., 2016) based on Trimmomatic (Bolger et al., 2014): (https://github.com/qczhang/icSHAPE/blob/master/scripts/trimming.pl):

```
perl trimming.pl −1 $fastq-file1 −2 $fastq-file2 -p $trimmed-file1 -q $trimmed-file2 -l 0 -t 0 -c phred33 -a adaptor.fa -m 36
```

The reads were then mapped using STAR (Dobin et al., 2013; Dobin and Gingeras, 2015) to the GRCh38 Ensembl genome, with Homo_sapiens.GRCh38.84.gtf annotations (http://uswest.ensembl.org/index.html), using the following command::

STAR–genomeDir ∼/genome/human/star–runThreadN 8–readFilesIn $trimmed-file1 $trimmed-file2–outFileNamePrefix $output-samfile

The mapped reads were then counted using HTSEQ (Anders et al., 2014):

python -m HTSeq.scripts.count -m intersection-nonempty -s reverse -i gene_id $output-samfile ∼/genome/human/Homo_sapiens.GRCh38.84.gtf > $txt

The mapped data was visualized using the UCSC browser track (Kent et al., 2002). To generate genome tracks we used samtools (Li et al., 2009) to generate stranded BAM files for each library from the SAM file. The BAM file was then used to generate a bedGraph following the command:

genomeCoverageBed -bg -split -ibam $bam -g ∼/genome/human/star/chrNameLength.txt > $bed_file

BedGraph files from multiple replicates were aggregated using bedtools (Quinlan and Hall, 2010) unionbedg and each track was normalized to the same sequencing depth (30 million reads each). The averaged bedGraph files were converted to BigWig files using command bedGraphToBigWig (Kent et al., 2010) for visualization in the UCSC browser (Karolchik et al., 2004). Statistics from the mapped data was aggregated using MultiQC (Ewels et al., 2016). To calculate FPKM (fragments per kilobase per million reads), we obtained transcript lengths from Biomart Ensembl (Durinck et al., 2005) (Ensembl Genes 92, GRCh38), using the longest stable isoform for a gene as its length.

Transcript-level quantification

Kallisto (Bray et al., 2016) (v 0.43.1) was used to quantify transcript-level abundances of the APEX-seq libraries. A fasta file corresponding to Homo_sapiens.GRCh38.89.gtf and hg38 was downloaded from the Ensembl website and a kallisto index was generated using the kallisto index command with default arguments. To quantify each pair of fastq files, the kallisto quant command with the -b 30 argument was used.

Data analysis using DESeq2

Differentially-expressed genes were determined using DESeq2 (Love et al., 2014), using FDR < 0.05 and 18 controls. We tested the effect of imposing other FDR (false discovery rate) cutoffs, and found no appreciable increasing in precision with further decreasing FDR to 0.01. However, increasing FDR beyond 0.05 dramatically decreased precision. All P values from DESeq2 are FDR adjusted for multiple-hypothesis testing.

For the OMM perturbation experiments, we used the same 18-control strategy, but replacing the unperturbed OMM APEX-seq and cytosol APEX-seq values with the corresponding drug-perturbed values. Using a strategy where we only had 4 controls per perturbation experiments (2 OMM unlabeled and 2 cytosol unlabeled) did not appreciably change the conclusions. For the nocodazole time course experiment we used controls generated at 3 min treatment to calculate enrichment values for the 3 min and 6 min target libraries, and controls generated at 30 min treatment for the 9 min, 30 min and 2 h target time points.

There were two exceptions to the 18-control approach in all our analysis. For the LMA gene in nuclear lamina, and the SENP2 gene in the nuclear pore construct, the unlabeled control had high counts for these genes in the RNA-seq data, as these genes were used to target APEX2 to the corresponding location. Therefore, to compensate, we replaced the LMA 18-control DESeq2 $\log_2$fold-change with the 2-control $\log_2$fold-change (using LMA controls) in the LMA data; we did the same for SENP2 in the nuclear pore dataset. Otherwise, all other data was as is. As the default DESeq2 approach (Love et al., 2014) replaces outliers when there are > 7 replicates, with our 18-control experiment we didn't need to change the corresponding DESeq2 values of sub-compartments other than nuclear pore and nuclear lamina.

Generating Orphan Lists

The orphan lists in Figure 2F include candidates from 7 locations – ERM, OMM, nucleus, nuclear lamina, nuclear pore, nucleolus and cytosol. We did not find any significantly-enriched transcripts in the KDEL, so no RNAs from this location were included in the orphan list. To generate the ERM and OMM orphan list, we started with the 1077 and 1027 enriched transcripts in ERM and OMM respectively and excluded all secretory genes. To generate the nucleus and cytosol orphan lists we started with the enriched genes from the atlas analysis (Figure 3D), and excluded all genes that were known to be enriched in these locations based on published fractionation-seq data from HEK293 (rRNA-depleted) (Sultan et al., 2014). For the fractionation-seq data the corresponding files were downloaded from the European Nucleotide Archive (accession number PRJEB4197), and processed identically to the APEX-seq fastq files. To validate nucleus and cytosol orphans, we carried out our own nuclear/cytosol fractionation, but using polyA+ selection and making RNA-seq libraries identically to the APEX-seq libraries.

To generate the nucleolus, nuclear pore and nuclear lamina orphan lists, we started with the genes from the atlas analysis and included genes that were highly-enriched in the location ($\log_2$foldchange > 0.75) relative to nucleus APEX-seq.

FPKM data sources

To obtain FPKM (reads per kilobase per million reads) of genes, we used two sources. First, we used published polyA+ data (Sultan et al., 2014) by averaging data from two protocols (Qiaquick and Trizol). The corresponding fastq files were downloaded from the

European Nucleotide Archive (accession number PRJEB4197), and processed identically to the APEX-seq fastq files. Second, we estimated FPKM from the raw counts from our 18-control samples. Briefly we calculated the FPKM for each control sample and averaged the FPKM values from all 18 controls. As the RNA-seq reads from unlabeled samples were obtained after treatment with streptavidin beads, these FPKM values might suffer from sequence- or length-dependent biases. However, genome-wide we found the data to be highly-correlated ($r = 0.95$) with the published data (Sultan et al., 2014). For the correlation analysis, we considered FPKM > 1. For all analyses that used FPKM values, we also only considered genes with FPKM > 1.

ERM APEX-seq extended analysis

We extensively tested the ERM APEX-seq dataset against the published ER fractionation (Reid and Nicchitta, 2012) and ER-proximal ribosome profiling (Jan et al., 2014) datasets. Briefly the ERM APEX-seq $\log_2$fold-changes were cytosol normalized by subtracting the corresponding cytosol (NES) $\log_2$fold-change. This ratiometric normalization increased specificity for challenging sub-compartments (Figures S2I) and is routinely used for APEX proteomics analysis (Hung et al., 2014). To test the specificity and sensitivity of ERM APEX-seq, we used receiver-operator-curve (ROC) (Linden, 2006).For the true positive list to test against, we considered the ~640 ER-enriched transcripts by ribosome profiling ($\log_2$fold-change > 0.904, as determined by authors), and the false positives were non-secretory RNAs – these were genes not in Phobius (Käll et al., 2004), SignalP (Petersen et al., 2011) and TMHMM (Krogh et al., 2001). In conjunction with our data, we also examined ER ribosome profiling data using ROCs, including transcripts with total RPKM > 10, as recommended by authors. From the ROC analysis, the cutoff was the value that maximized the difference between the true positive rate (TPR) and false positive rate (FPR). For ERM APEX-seq we explored different analysis approaches, including using 2-controls (ERM APEX-seq controls), 4-controls (ERM and cytosol APEX-seq controls) and 18-control samples. We also explored including or excluding ratiometric normalization (i.e., cytosol normalization to reduce background). We finally settled on the 18-control condition based on high specificity and reasonably-high coverage (>1,000 enriched genes). For this 18-control experiment, DESeq2 $\log_2$fold-change values from cytosol APEX-seq were subtracted from ERM APEX-seq to obtain ratiometric normalization (ERM/cytosol), and a final cutoff of $\log_2$fold-change (ERM/cytosol) > 0.8725 was obtained from the ROC. Unlike the published studies (Jan et al., 2014; Reid and Nicchitta, 2012), we didn't need to use CHX to stabilize transcripts.

Our analysis suggested improved performance (i.e., specificity) when combining replicates, especially when dealing with challenging/open sub-compartments. As few as 4 controls can improve performance. However, combining controls from multiple constructs/experiments is typically unnecessary when dealing with closed sub-compartments such as the nucleus, cytoplasm or mitochondrial matrix.

To compare the abundance of transcripts recovered by ERM APEX-seq, ER fractionation and ER ribosome profiling, we used a published HEK293 polyA+ RNA-seq dataset (Sultan et al., 2014). To estimate the coverage of our ER datasets, we chose a reference gene list comprising of 71 mRNAs that encode ER resident proteins, as previously described (Kaewsapsak et al., 2017). For the comparison of coverage with ERM proteomics, we used the published dataset containing gene names (Hung et al., 2017).

Nucleus (NLS) APEX-seq extended analysis

To validate the NLS APEX-seq orphans we carried out nuclear fractionation of HEK293T cells by following an established protocol (Gagnon et al., 2014). The protocol uses a detergent nonidet P40 (NP-40) to separate ER contaminants from the nucleus, and we confirmed this strategy was effective by imaging isolated nuclei, staining for ER using ER tracker Red (BODIPY TR Glibenclamide – Thermo Fischer), and visualizing on fluorescence microscope (Zeiss Observer Z1). We modified the protocol so that the extracted RNA was not purified by trizol extraction, but rather by using the RNeasy plus mini kit (QIAGEN). RNA-seq was carried out using the same protocol as that used for APEX-seq, thereby generating polyA+ libraries for the nuclear and cytoplasmic fraction using Illumina TruSeq kit. All experiments were carried out in biological replicates.

To estimate precision and accuracy of NLS APEX-seq, we used our polyA+ fractionation-seq data to generate true-positive and false-positive lists. We did so by first obtaining transcripts differentially expressed in the nuclear relative to cytoplasmic fraction ($p_{\text{FDR-adjusted}} < 0.05$), and did the same for nucleus (NLS) APEX-seq versus cytosol (NES) APEX-seq. We categorized transcripts into the following categories (Figure 2G): (1) $\log_2$fold-change NLS > 0 and $\log_2$fold-change (nuclear/cytosolic fractionation) > 0 (true positive; TP), (2) $\log_2$fold-change NLS > 0 and $\log_2$fold-change (nuclear/cytosolic fractionation) < 0 (false positive; FP), (3) $\log_2$fold-change NLS < 0 and $\log_2$fold-change (nuclear/cytosolic fractionation) > 0 (false negative; FN), (4) $\log_2$fold-change NLS < 0 and $\log_2$fold-change (nuclear/cytosolic fractionation) < 0 (true negative; TN). Precision was defined as TP/(TP+FP), accuracy as (TP+TN)/(TP+TN+FP+FN), sensitivity as TP/(TP+FN), and specificity as TN/(TN+FP). Transcripts shorter than 100 nt were excluded from analysis. We calculated precision and accuracy for all transcripts, as well as for ER-transcripts (those enriched by ERM APEX-seq) and non-ER transcripts. Other analysis approaches (using other log2foldchange cutoffs, making receiver-operator-curves etc.) did not change the main conclusions.

OMM APEX-seq extended analysis

For OMM APEX-seq data in Figures 6 and 7, a similar ratiometric normalization to ERM with cytosol was carried out. Based on extensive testing with ERM APEX-seq and nucleus APEX-seq using the corresponding known gene-lists, we found that in general a default $\log_2$fold-change cutoff of 0.75 was suitable for dealing with APEX-seq when prior knowledge was unavailable, or un-assumed. We therefore used $\log_2$fold-change (OMM/cytosol) = 0.75 as a cutoff to identify OMM-enriched transcripts.

For labeling secretory RNAs (Figure S3D), we identify and display secretory RNAs in this order (1) first all Phobius, (2) TMHMM but not Phobius, (3) SignalP but not Phobius or TMHMM (4) Gene ontology cellular component (GOCC) but not Phobius, TMHMM or SignalP. Mitocarta2.0 were excluded from secretory RNA (own category).

Mitochondria drug perturbation

For cycloheximide treatment, APEX labeling in OMM-APEX2 stable cells was initiated by changing the medium to fresh medium containing 500 mM biotin-phenol. This was incubated at 37°C under 5% CO_2 for 15 min. Then cycloheximide (Sigma Aldrich) was added to the medium to a final concentration of 0.1 mg/mL and the cells were further incubated at 37°C under 5% CO_2 for another 15 min. H_2O_2 was then added to each sample to a final concentration of 1 mM, and the plate gently agitated for 1 min. Then the samples were quenched and processed the same way as other APEX-seq samples. For puromycin or CCCP experiment, APEX labeling in OMM-APEX2 stable cells was initiated by changing the medium to fresh medium containing 200 μM puromycin (VWR) (or 40 μM CCCP [Sigma Aldrich]) and 500 mM biotin-phenol. This was incubated at 37°C under 5% CO_2 for 30 min. H_2O_2 was then added to each sample to a final concentration of 1 mM, and the plate gently agitated for 1 min. Then the samples were quenched and processed the same way as other APEX-seq samples.

For the nocodazole experiments, we added 10 μM nocodazole (Sigma Aldrich) to fresh media and incubated cells for 3, 6, 9, 30 and 120 min 37°C under 5% CO_2, followed by 1 min labeling by adding H_2O_2 at room temperature to a final concentration of 1 mM. Biotin-phenol was added to the media 30 min prior to labeling. Samples were quenched and processed the same way as other APEX-seq samples.

OMM perturbation data analysis

For gene classification, mitochondrial genes were annotated according to MitoCarta 2.0 (Calvo et al., 2016); secretory genes were annotated as in Kaewsapsak et al. (2017) according to Phobius, SignalP, TMHMM, GOCC and ER proximity ribosome profiling. For mitochondrial genes, we adapted the original TargetP algorithm prediction score (0 = no targeting sequence, 1-5 from strongest to weakest) to a different scale (0 = no targeting sequence, 1-5 from weakest to strongest) as a metric of the strength of N terminus mitochondrial targeting sequence. The mitochondrial gene functional classes were annotated according to Gene Ontology and are listed in Table S4. For the gene density plots in Figures 6B and 6C, all detected transcripts in each condition were plotted by their $\log_2$fold-change normalized against their respective cytosol control using a bin size of 0.2. For the functional class analysis in Figures 6F and 6G, the top 100 enriched mitochondrial genes in each experiment were selected based on MitoCarta 2.0 for mitochondrial annotation and $\log_2$fold-change of OMM values normalized against their respective cytosol control.

To calculate nocodazole half-lives the non-linear regression function *nls* in R was used. We excluded transcripts with half-lives shorter than 0.5 min, and longer than 60 min as these were not reliable. We obtained half-lives for 461 of the 768 transcripts in Cluster 2 (Figure 7K).

Empirical classification of OMM-localized transcripts as ribosome- or RNA-dependent

OMM-enriched transcripts from the heatmap (N = 1902, Figure 6M) who abundance increased with cycloheximide treatment and decreased with puromycin treatment were considered to be ribosome-dependent. In contrast, transcripts whose enrichment at the OMM was largely unchanged following puromycin or cycloheximide treatment were considered to localize in an RNA-dependent manner. The separation of these two populations of RNAs is shown in Figure 7A.

Prediction localization to the OMM versus ERM

If RNA-dependent transcripts localize based on their RNA sequence, and ribosome-dependent transcripts localize based on their protein sequence, a prediction that follows is that the RNA sequences of RNA-dependent transcripts are somehow more distinguishable from non-OMM-localized transcripts than ribosome-dependent transcripts. In other words, if cellular machinery recognizes the sequence of RNA-dependent transcripts and their RNA sequences are sufficient for RNA localization, then the localization to the OMM, as opposed to another cellular destination, should be more predictable based on RNA sequence for these transcripts relative to ribosome-dependent transcripts. We therefore hypothesized that a machine learning classifier would be more able to classify transcripts as being OMM-localized or ERM-localized when comparing ERM-enriched transcripts to ribosome-dependent transcripts, than when comparing ERM-enriched transcripts to protein-dependent transcripts. The ERM was chosen as a dataset to compare with as the ERM and OMM are physically proximate in cells, and both localizations where translation occurs.

To test this hypothesis, we used a random forest model to classify transcripts as being OMM- or ERM-localized. Broadly, training inputs were a list of transcripts and their empirical classification (OMM or ERM), and test inputs were a list of withheld transcripts whose predicted classification (OMM or ERM) was compared with their empirical classification. Model performance was compared when using OMM RNA-dependent transcripts and ERM transcripts, versus OMM ribosome-dependent transcripts and ERM transcripts.

OMM RNA-dependent and ribosome-dependent gene lists were identified as described above. ERM-localized genes were identified based on: $\log_2$FC enrichment > 0.75, adjusted p value < 0.05, and $\log_2$FC enrichment in ERM $>$ $\log_2$FC enrichment in OMM. Any genes in the ERM list that were also present in the OMM lists were excluded (from both lists), such that only uniquely localized genes were included for classification. The most abundant transcript isoform in the control samples was used as the primary transcript whose sequence was used for downstream analysis. Transcript sequences were converted into kmer counts by 1) generating a list of all possible kmers of a given *k*, 2) counting the number of times that kmer was present in a given transcript sequence, and 3) normalizing the kmer counts for a given transcript by the length of that transcript (i.e., this results in the relative per-transcript abundance of all possible kmers). For comparisons based on RNA-localization (Figure 7B), a *k* of 6 was used, resulting in 4096 (4^6) possible kmers. When comparing the sequences of only UTRs or CDS, only transcripts containing a 5′UTR/CDS/3′UTR sequence of at least length 10 were used.

The ensemble.RandomForestClassifier in the Python scikit-learn package (v 0.20.0) was used with default settings, with the exception of: *n_estimators = 100*, *max_features = 4096*, *min_samples_split = 15*, *min_samples_leaf = 15*. 10-fold cross-validation was used. ROC curves were generated using the ensemble.RandomForestClassifier.predict_proba() and metrics.roc_curve() functions in scikit-learn. Mean ROC curves are shown, with shaded areas indicating one standard deviation.

To test the hypothesis that OMM ribosome-dependent transcripts should be more predictive based on their protein sequence than OMM RNA-dependent transcripts, the above procedure was also performed using the protein sequences of ERM-localized, OMM P, and OMM R transcripts. Only protein-coding transcripts were used. As there are a greater number of possible amino acid kmers (22^k) than nucleic acid kmers (4^k), a *k* of 3 was used, and only kmers found at least twice across all protein sequences (in any one of the three lists) were included in downstream analyses. The use of a smaller *k* and/or the greater number of possible amino acid sequences, in addition to potential biochemical similarities between certain sets of amino acids (e.g., hydrophobic amino acids) which may be biologically similar but are not explicitly included in our model, may contribute to lower performance relative to classification based on RNA sequence. As protein-dependent localization would be predicted to be primarily dependent on the N-terminal amino acids, as these are the amino acids displayed during nascent peptide synthesis, only the first 100 N-terminal amino acids were used. Proteins whose sequences were shorter than 40 amino acids were excluded. The restriction to the 100 N-terminal amino acids is consistent with and based on the methods used by other signal peptide prediction programs (i.e., TargetP).

Random forest classification of OMM transcripts as RNA-dependent or ribosome-dependent

To validate the random forest model classification of OMM-localized transcripts as being RNA-dependent or ribosome-dependent (P transcripts), the ensemble. RandomForestClassifier was used as described previously (with the same settings) and 10-fold cross-validation (Figure 7D). Subsequently, to determine relative kmer importances, the entire dataset of RNA-dependent and Ribosome-dependent transcripts (with no transcripts withheld) was used to train the model (using per-transcripts length-normalized 6-mer counts of all 4096 6mers). Feature importances were normalized to the maximum feature importance. These 6-mer importances were then projected onto transcript sequences for all three gene lists (with overlapping genes not withheld), to identify the relative importance of transcript 6mers as a function of the position along the length of the transcript (i.e., to determine whether there exists a positional bias, such as 5′ or 3′ bias, in the part of the transcript most important for predicting RNA localization). To generate the relative importances, 1) the per-base importance of each transcript was initialized to 0, 2) transcripts were broken into consecutive 6mers, 3) the feature importance of each 6-mer was added to the 6 corresponding bases of the RNA transcript, to result in a per-base importance for each transcript. This was then normalized for each transcript to the maximum per-base importance, such that the values for each transcript range from 0 to 1. A sliding average window of 20-bases was used and the resulting importances were then normalized based on transcript length to create the metaplot shown in Figure S7B, such that the position importances for each transcript ranged from 0 (representing the 5′ end of a transcript) to 1 (the 3′ end of a transcript).

PolyA score prediction and polyA-tail length

The polyA_SVM package (v.2.2) (Cheng et al., 2006) was used to compute predicted polyadenylation site scores for all transcripts using default settings. The maximum predicted score for each transcript was used. If no predicted score was returned (i.e., the polyA_SVM package did not predict the presence of a polyA site), then a score of 0 was used. The sequences of the three respective gene lists (ERM-localized, OMM RNA-dependent transcripts, and OMM ribosome-dependent transcripts) generated as described previously were used, and overlapping transcripts (found in both the ERM and OMM lists) were not excluded. The polyA tail length data was obtained from GSE52809 (Subtelny et al., 2014).

Correlation and T-distributed stochastic neighbor embedding (t-SNE) analysis

For the 9-location correlation and t-SNE (van der Maaten and Hinton, 2008) analysis we only included genes with average counts per sample greater than 100 across all 36 samples (2 labeled targets and 2 unlabeled controls per location). We excluded genes with transcript length less than 100 nt. The raw counts from HTSEQ were rlog-transformed using DESeq2-normalized counts. Pearson correlation on the transformed counts was carried out using the package corrplot in R, using clustering method “centroid” and order “hclust.” t-SNE analysis was also performed in R. For the targets-only t-SNE we included genes with average counts per sample greater than 1000 across all 18 samples (2 labeled targets per location).

For the OMM drug-treatment experiments, we only included genes average counts greater than 100 per sample across 32 samples (2 labeled targets and 2 labeled controls for the following: OMM_basal, OMM_cycloheximide, OMM_puromycin, OMM_cccp, cytosol_basal, cytosol_cycloheximide, cytosol_puromycin, cytosol_cccp). All other analyses were carried out identically to the 9-location analysis.

Heatmap and gene-ontology (GO)-term analysis

For the integrated analysis of locations, we excluded MITO APEX-seq as the labeled targets perturbed the entire analysis; we believe this is due to the large enrichment of ~13 mitochondrial mRNAs and 2 rRNAs, which constitute over 50% reads in targets; combined with the relative spatial isolation of the matrix.

To generate reliable gene data for the integrated analysis, we took our APEX-seq enrichment data and imposed the following filtering criteria: (1) excluding transcripts shorter than 100 nt that were not recovered efficiently. (2) Considering transcripts with common gene names (typically HUGO gene nomenclature committee [HGNC] approved names; Maglott et al., 2011; Pruitt et al., 2007) (3) only including genes that were enriched in at least 1 location ($p_{\text{FDR-adjusted}} < 0.05$ and $\log_2$fold-change > 0.75 for at least 1 location); and (4) Genes had $\log_2$fold-change data estimated from DESeq2 for all locations (i.e., excluding any genes with NA values in any location). This last filtering step typically excluded low-abundant transcripts that might occasionally show up as enriched in a location but didn't have sufficient counts in other locations. Such low-abundant transcript-data was typically less reliable. We did not impose any FPKM or counts cutoff in our analysis. Our analysis yielded 3262 genes, shown in Table S3. As the fold changes in this study were calculated relative to unlabeled controls, enrichment by APEX-seq is a proxy for transcript concentration. Thus, the cytosol, which constitutes most of cell, recovers fewer transcripts than expected, as it is not possible to highly concentrate transcripts there.

Heatmaps of this data were generated using pheatmap2 in R, with default settings. From the heatmap, clusters were estimated using hierarchical clustering. The cluster number was checked using a number of approaches including gap statistics (Tibshirani et al., 2001), and the combined cluster range was then explored. The genes belonging to each cluster was then compared to all enriched genes to estimate cellular GO-terms. GO-term analysis was carried out using PANTHER (Mi et al., 2013; Thomas et al., 2003) (http://pantherdb.org/about.jsp), using Fischer's exact test with FDR multiple test correction. We only consider GO-terms with FDR < 0.005. To construct the heatmaps of most variable mRNAs (Figure 3E), we considered genes with average counts > 1000. For the lncRNA heatmap (Figure 3F), we excluded all genes that were not lncRNAs, processed transcripts and pseudogenes.

We took a similar approach for making heatmaps was used for the OMM analysis with the drug perturbations (puromycin, CCCP, cycloheximide). However, for clustering we did not use CCCP data. For the subsequent GO-term analysis we used the Reactome pathway from PANTHER, with the control set comprising all genes enriched in at least one of the 4 OMM APEX-seq conditions (~1900 genes).

Nuclear-locations m^{6}A modification and length analysis

To examine transcript-length differences across the nuclear locations (nucleus, nucleolus, nuclear pore, nuclear lamina), we filtered genes as described above for the heatmaps, but we excluded the filtering step by common gene names. Our analysis yielded 3288 genes. We obtained transcript lengths from two sources: (1) The longest stable isoform, as obtained from Biomart, Ensembl (Durinck et al., 2005), and (2) the most-abundant isoform across all compartments in our APEX-seq data, as determined by rMATs (Shen et al., 2014). Using the transcript length from either of these databases yielded similar trends and conclusions.

To determine the contribution of 5′ UTR, CDS (coding sequence) and 3′ UTR to the overall transcript-length difference between nucleus- and nuclear-pore enriched transcripts, we considered the most-abundant isoform, but excluded non-coding transcripts (i.e., transcripts with a CDS length = 0).

To calculate the number of m^{6}A sites per transcript, we used a published dataset to obtain high-confidence m^{6}A sites in HEK293 (Meyer et al., 2012).

Network analysis

RNA interactions for the 3262 genes were investigated in multiple ways. These include (1) tabulating the overlapping genes using UpSet (Lex et al., 2014) in R; and (2) using circlize (Gu et al., 2014) to investigate the data by comparing which transcripts in each cellular sub-compartment most often had residency in other locations. In all instances the fold change for all genes for all transcripts was binarized to either 1 ($\log_2$fold-change > 0.75), else 0.

Lamin-associated domains (LADs) and nucleolus-associated domains analysis

For the LADs and NADs analysis, we aggregated data from the following sources to obtain the relevant associated genomic regions: Guelen et al. (2008), Dillinger et al. (2017), Németh et al. (2010). We used library ((TxDb.Hsapiens.UCSC.hg18.knownGene) in R, obtained from Bioconductor (Durinck et al., 2005; Gentleman et al., 2004) to get the genes contained within these regions.

Quantification of intron retention and intron switching

rMATS (Shen et al., 2014) was used to quantify intron retention in each location. rMATS was run by comparing the APEX-seq BAM files against all controls using the arguments -t paired, and a GTF file downloaded from Ensembl (Genecode v26, Ensembl 88). Only retained intron events with FDR $\leq$ 0.05 were considered using the ''RI.MATS.JCEC.txt'' output file (using both junction and exon counts).

rMATs (v 4.0.1) was used to quantify the number of isoform-switching genes (Figures S5F and S5G) in the APEX-seq labeled samples relative to all unlabeled controls. The number of significant differential-splicing events (FDR < 0.05) for each compartment was read from the rMATs JCEC files. To remove noise from low-abundance transcripts, the KDEL labeled sample was used as a filter. Any differential splicing events identified in the KDEL labeled samples were ignored, as previous analysis using DESEQ2 found no significantly-enriched genes at that location. The number of genes containing at least one differential splicing event between a labeled compartment and unlabeled controls are reported for the respective alternative splicing event.

Isoform analysis, including isoform switching

Sleuth (Pimentel et al., 2017) was used to perform differential transcript expression analysis between locations, which were compared against all control samples. For the analyses in identifying isoform switching, to generate gene-level abundances the Bioconductor (Gentleman et al., 2004) tximport package was used to import kallisto (Bray et al., 2016) abundances and aggregate to the gene-level. DESeq2 (Love et al., 2014) was subsequently used to perform differential gene expression analysis. Genes that displayed isoform switching were identified as follows: First, using the differential gene expression output from DESeq2, genes displaying no significant differential expression between the nucleus (NLS) and cytosol (NES) samples were identified. For each of these genes, we then determined if there were any transcripts that were significantly enriched in either the nucleus or cytosol samples (as determined by Sleuth [Pimentel et al., 2017]). Genes displaying no differential expression between the nucleus and cytosol, but with at least one transcript enriched in the nucleus and a different transcript enriched in the cytosol, were called as displaying isoform switching. To select genes to display in Figure 5E, an expression cutoff (at the gene level) of $\log_2$counts > = 12 and an isoform difference metric > = 10 was set. The isoform difference metric was computed by taking the sum of the absolute values of the $\log_2$fold-change enrichments for the most cytosol-biased and most nuclear-biased transcript.

Repeat analysis

A list of all annotated repeat elements was downloaded from UCSC Table Browser (Karolchik et al., 2004). To determine the relative enrichment of repeat elements in the genes enriched in each location, a set of enriched genes in each location was determined as described previously ($\log_2$fold-change > = 0.75, $p_{FDR^-adjusted} < 0.05$). A unique set of genes for each location was determined by removing genes that were enriched in more than one APEX-seq location.

For each set of genes, a corresponding list of genomic coordinates comprising only exonic sequences was generated. The most abundant isoform of each gene was used for determining the coordinates of the exons. This list was then intersected with the repeat annotation using bedtools (Quinlan and Hall, 2010) intersect with the -F 0.51 command to require that at least half of the repeat annotation was present in an exonic sequence. This was then aggregated by gene to generate a “repeat count” by gene table (with all repeat families as rows, and all genes uniquely enriched in a given location as columns). This table was then binarized to result in a table reporting the presence or absence of a repeat element in each gene. The proportion of genes in each location that contained a given repeat family was then determined. To perform FDR calculations, the gene-location pairings were randomly permuted 1000 times, and the number of permutations in which the resulting enrichment value was at least as great as the observed enrichment value was divided by the total number of permutations.

To quantify the abundance of rRNA repeat elements, the same list of all annotated repeat elements from UCSC (Karolchik et al., 2004) was used (typical size $10^2 – 10^3$ bp). The number of reads mapping to any rRNA element for each location was determined using bedtools intersect, essentially using the rRNA repeat annotations as a “gene” or “feature” to quantify overall abundance. These values were depth normalized to the total number of aligned reads in each BAM file, and averaged across replicates.

Sequential fluorescence *in situ* hybridization (FISH) design and analysis

Sequential oligo library for 56 selected genes, which include a combination of known and previously-unknown-location genes, was designed according to Moffitt and Zhuang (2016) and synthesized by CustomArray. The library was then PCR amplified using Phusion Hot-start Master Mix (NEB, M05365) and then cleaned up using DNA clean and concentrator −5 columns (DCC-5, Zymo Research, D4013). The library was then in-vitro transcribed with T7 polymerase using the HiScribe kit (NEB, E20505) at 37°C overnight. The resulting RNA was then reverse transcribed with Maxima H Minus RT enzyme (ThermoFisher, EP0751) at 50°C for 1 h and the remaining RNA digested with 0.25 M EDTA and 0.5 M NaOH at 95°C for 10 min. The correct size of the reverse transcribed RNA was confirmed by running the product on a 15% urea TBE gel. The probes were further cleaned up using DCC-25 columns (Zymo Research, D4005).

To hybridize FISH probes on to cells, HEK293T cells were fixed with 4% paraformaldehyde (PFA) in PBS for 10 min before permeabilized with 0.5% Triton-X in PBS for 10 min. The sample was then incubated in 50% formamide and 0.1% TWEEN 20 in 2X SSC solution for 35 min. 500-800 ng/μL of the synthesized probe were added onto the cells using a coverslip and the slides were denatured at 90°C for 10 min. Probes were hybridized overnight at 42°C in a humidified chamber. The cells were then washed twice with prewarmed 42°C 2XSSC solution for 10 min the next day before imaging on a confocal microscope. A total of 14 fields of view, each with > 20 cells, were imaged for all 56 genes and then the data were processed using MATLAB. Using the FISH images generated for each demultiplexed transcript, we subsequently excluded transcripts that (1) could not be decoded based on the barcode, or (2) that didn’t show any localization (typically low-abundant ones) based on the images being hazy and lacking punctate spots. To carrying out this exclusion in a relatively unbiased manner, we had 3 people (F.M.F., S.H., K.R.P.) independently examine the images for all genes, and rate transcript-localization information as (1) high confidence (2) medium confidence and (3) low/no confidence. We then tallied all these ratings and subsequently excluded transcripts that were assigned a “no confidence” value by any of the 3 people. In general, the 3 people strongly agreed on the confidence ratings. We separately also confirmed that for transcripts with known localization, the discarded genes did not correlate well with known localizations. For imaging quantitation and analysis of each field of view, we generated a mask for each individual gene of interests using a uniform threshold cutoff of 0.5 – 0.998 after removing all the non-cell pixels. The colocalization with *MTND3* was calculated by intersecting the mask of a particular gene of interest (for example, "*XIST*" mask) with *MTND3* mask and then divided sum intensity of the intersected mask by the sum intensity of the gene mask of interests. Colocalization with ERM marker SCD was calculated using the same approach. The colocalization results for all 14 fields of view were then calculated to obtain the average and standard deviation.

MITO APEX-seq extended analysis

For the MITO APEX-seq, we obtained strong enrichment ($\log_2$fold-change > 2.9) of the 13 MT mRNAs and 2 MT rRNAs in the targets (i.e., labeled libraries) relative to unlabeled controls. These 15 genes made up > 50% of reads in the MITO APEX-seq labeled samples.

In addition to the 15 expected mitochondrial RNAs, we also recovered ∼400 transcripts that were moderately enriched ($\log_2$fold-change > 0.75), some of which are known mitochondrial pseudogenes. To rule out that this labeling was not because the biotin-phenoxy radical, generated during the labeling experiment, was escaping from the mitochondrial matrix we confirmed that OMM APEX-seq enriched transcripts (> 1000-enriched transcripts) showed no enrichment (average $\log_2$fold-change ∼0) in the MITO APEX-seq samples. While we do not believe these transcripts to be present in the mitochondrial matrix (Mercer et al., 2011), attempts to confirm the localization by FISH were not successful. We hypothesize two explanations for the observations: (1) Due to the large perturbation introduced by APEX-seq labeling, the DESeq2 analysis does not perform properly; or (2) There is some small background labeling by Cox4-APEX (i.e., MITO-APEX) as the protein makes it way from the cytosol, where it is translated, to the mitochondrial matrix.

NES APEX-seq extended analysis

We did not find many transcripts highly enriched ($\log_2$fold-change > 0.75) by cytosol (NES) APEX-seq. We believe fewer transcripts are recovered because APEX-seq enrichment is a proxy for RNA concentration rather than RNA amount. Thus, the cytosol, which contains a majority of transcripts, recovers fewer highly-enriched transcripts relative to the unlabeled (i.e., whole-cell) controls. Nonetheless we compared the transcripts enriched by cytosol APEX-seq (log2foldchange > 0, $p_{\text{FDR-adjusted}} < 0.05$) and found them to have higher enrichment in the cytosol fractionation fraction relative to transcripts with cytosol APEX-seq $\log_2$foldchange < 0.

KDEL APEX-seq extended analysis

For the KDEL construct, DESeq2 did not show any significantly enriched transcripts relative to unlabeled controls, when FDR adjusted. If there are any significantly-enriched transcripts larger than 100 nt, they are few in number. We therefore used the KDEL APEX-seq data as a "negative control" our 8-location integrated analysis by rejecting analysis strategies that yield a large number of enriched KDEL transcripts, as such approaches likely have large false positives. We found that using a $\log_2$fold-change between 0.6 and 0.9 was a sufficient compromise to obtain highly-specific gene lists without further loss of coverage (Figure S2M).

Proteomic analysis

For the proteomic analysis, we used subcellular protein localization data from Thul et al. (2017), using the main location for genes that were imaged using validated and supported antibodies. We filtered the data to exclude duplicate protein localization entries from multiple cell-lines. The majority of the proteins in that dataset are nucleoplasmic or cytosolic. We calculated an "enrichment" score for each protein type in each location by carrying out a two-step normalization: (1) obtaining the enrichment of that protein type relative to all proteins, and (2) enrichment of that protein in each location relative to all locations.

Other analysis and data availability

Where appropriate, the following tests were employed (1) Student's t test, (2) Mann-Whitney U test (Wilconox rank-sum test) (3) Kolmogorov–Smirnov (KS) test, (4) Fischer's exact test, (5) hypergeometric distribution test. All tests were carried out in R. All analysis was carried out using R (most plots using ggplot2; Wickham, 2009), python and Microsoft Excel. All custom code used in this work is available upon request. All sequencing data are available through the Gene Expression Omnibus (GEO) under accession GSE116008. Browser tracks can be found at: https://genome.ucsc.edu/cgi-bin/hgTracks?hgS_doOtherUser=submit&hgS_otherUserName=krparker&hgS_otherUserSessionName=APEXseq_all_stranded (stranded RNA-seq) and https://genome.ucsc.edu/cgi-bin/hgTracks?hgS_doOtherUser=submit&hgS_otherUserName=krparker&hgS_otherUserSessionName=APEXseq_all_unstranded (unstranded RNA-seq).

DATA AND CODE AVAILABILITY

All data presented are available in the main text and supplementary materials. Browser tracks can be found at: https://genome.ucsc.edu/cgi-bin/hgTracks?hgS_doOtherUser=submit&hgS_otherUserName=krparker&hgS_otherUserSessionName=APEXseq_all_stranded (stranded RNA-seq) and https://genome.ucsc.edu/cgi-bin/hgTracks?hgS_doOtherUser=submit&hgS_otherUserName=krparker&hgS_otherUserSessionName=APEXseq_all_unstranded (unstranded). The accession number for the raw sequencing data reported in this paper is Gene Expression Omnibus (GEO): GSE116008.